Extension and Inversion of Salt-Bearing Rift Systems

Tim P. Dooley & Michael R. Hudec

Applied Geodynamics Laboratory, Bureau of Economic Geology, Jackson School of Geosciences, University Station Box X, Austin Texas 78713, USA

Abstract:

We used physical models to investigate the structural evolution of segmented extensional rifts containing syn-rift evaporites and their subsequent inversion. An early stage of extension generated structural topography consisting of a series of en-échelon graben. Our salt analog filled these graben and the surroundings before continued extension and, finally, inversion.

During post-salt extension, deformation in the subsalt section remained focused on the graben-bounding fault systems whereas deformation in suprasalt sediments was mostly detached, forming a sigmoidal extensional minibasin system across the original segmented graben array. Little brittle deformation was observed in the post-salt section. Sedimentary loading from the minibasins drove salt up onto the footwalls of the subsalt faults, forming diapirs and salt-ridge networks on the intra-rift high blocks. Salt remobilization and expulsion from beneath the extensional minibasins was enhanced along and up the major relay/transfer zones that separated the original sub-salt grabens, forming major diapirs in these locations.

Inversion of this salt-bearing rift system produced strongly decoupled shortening belts in basement and suprasalt sequences. Suprasalt deformation geometries and orientations are strongly controlled by the salt diapir and ridge network produced during extension and subsequent downbuilding. Thrusts are typically localized at minibasin margins where the overburden was thinnest and salt had risen diapirically on the horst blocks. In the subsalt section, shortening strongly inverted sub-salt grabens, which uplifted the suprasalt minibasins. New popup structures also formed in the subsalt section. Primary welds formed as suprasalt minibasins touched down onto inverted graben. Model geometries compare favorably to natural examples such as those in the Moroccan High Atlas.

1. Introduction

As noted by Bonini et al. (2011), in their review paper, "basin inversion" is a commonly used term to signify shortening of formerly extensional basins (cf. Buchanan and McClay, 1991; Buchanan and Buchanan, 1995; Ziegler, 1987). Localization of shortening by extensional rifts, and their subsequent inversion, is not surprising as these are long-lived crustal weak zones. Inversion of graben and entire rift systems has been a significant focus of study since the early 1980s owing to its importance related to: (1) the role of pre-existing faults in focusing and accommodating shortening of the upper, shallow crust; (2) the role of pre-inversion high-angle faults as potential seismogenic sources and hazards, and; (3) their economic importance related to focused fluid flow and associated ore deposit generation was well as influencing hydrocarbon maturation, migration pathways, and trapping in inverted petroleum-bearing sedimentary basins (see Bonini et al., 2011 for further details and references). Deposition of evaporites in these

systems, either as syn-rift deposits or immediately after rifting, can add complexity to the system in many ways. For example salt may have significant variation in thickness across the rift resulting in varying degrees of coupling between the basement and suprasalt sediments during subsequent extension and inversion (e.g. Withjack and Calloway, 2000). Salt may also be expelled from beneath depotroughs, during extension and/or loading to form diapir networks that may later focus shortening as plate motions evolve (e.g. Dooley et al., 2005). These diapir networks may be surrounded by patchy weld systems adding further complications to the system (cf. Rowan and Krzywiec, 2014).

Examples of basement-involved inverted salt-bearing rifts include the the Mid-Polish Trough (e.g. Krzywiec, 2012; Rowan and Krzywiec, 2014), the southern North Sea (e.g. Stewart, 2007; Stewart and Coward, 1995; Davison et al., 2000; Jackson and Stewart, 2017) and the High Atlas of Morocco (e.g. Saura et al., 2014; Domenech et al., 2016; Martín-Martín et al., 2016; Moragas et al., 2017; Teixell et al., 2017; Verges et al., 2017; Figure 1). The central High Atlas range is a doubly-vergent fold-thrust belt that formed by inversion of a Triassic-Jurassic rift basin during the Alpine orogeny (e.g. Teixell et al., 2003; Saura et al., 2014; Moragas et al., 2017). Within the central part of the range outcrop is dominated by Lower-Middle Jurassic deposits that form brand synclines or flat-topped plateaux, and separated by NE-SW oriented anticlines or thrust faults (Figure 1; Moragas et al., 2017). These ridges have had a variety of explanations for their origin such as transpressional deformation or the emplacement of Jurassic intrusions (see detailed discussion in Moragas et al., 2017, for more details). A few studies of individual structures proposed a diapiric origin for these ridges (e.g. Michard et al., 2011). However, more recent studies have interpreted the entire Central High Atlas as a complex salt-bearing rift basin with

associated diapirism and minibasin formation, that was inverted in the Alpine orogeny. For example, Saura et al. (2014) documented more than ten elongated extensional minibasins that were originally separated by, now welded, salt walls. Thick evaporitic successions were deposited within the developing rift in the late Triassic (Verges et al., 2017). Extension continued into the Early Jurassic with coeval diapirism and minibasin formation, followed by a long post-rift stage where halokinetic processes continued to evolve (Moragas et al., 2017; Martín-Martín et al., 2016). Inversion began in the late Cretaceous (Domenech et al., 2016), squeezing a complex diapir and minibasin province. Such a diapir and minibasin province is likely to exhibit extreme variations in overburden strength, and thus behavior, during shortening. It is this salt-tectonic scenario that formed the inspiration for our experimental study.

Many experimental studies of contractional tectonics utilize silicone polymer as a detachment, sometimes with spatially variable and multiple detachment levels, usually of uniform thickness, in thrust belt studies (e.g. Couzens-Schultz et al., 2003; and see the review by Graveleau et al., 2012). Some previous physical modeling studies of basement-involved extension and inversion of salt-bearing rifts include those of Dooley et al. (2005) with application to the North Sea, and Moragas et al. (2017) in their focused study on syn- and post-rift diapirism and inversion in the Moroccan High Atlas. Bonini et al. (2011) modeled detached extension and subsequent shortening of these graben, Soto et al. (2007) modeled the effects of high-level ductile detachments above a variety of listric fault geometries, and Roma et al. (2017, 2018a, b) as well as Ferrer et al. (2014, 2016) modeled extension and inversion above rigid planar and ramp-flat extensional master faults with high-level and variable-thickness salt layers. However, all the basement-involved inversion studies to date relied on non-deformable basement blocks to

generate extension and subsequent inversion. An exception to this are the clay models of Durcanin (2009), but these models could not be sectioned and thus sections shown in this study are "hypothetical". A new series of experiments was designed to produce segmented rift systems in deformable model materials, fill them with syn-rift evaporites and subject them to further extension, loading and, finally, inversion. Our goals with these models was to test: (1) where and why do diapirs form in a segmented extensional rift system?; (2) how much coupling is there between basement and cover separated by a relatively thick salt body during extension and contraction?; (3) what styles of shortening structures form in the suprasalt section during inversion and what controls their location and style?, and; (4) what are the styles of shortening in the subsalt section and can we get significant reactivation of extensional structures during inversion?

2. Modeling Methodology

2.1 Model Design and Scaling

Our goal with these models was to generate a series of en-échelon graben across a rift system in a similar fashion to models presented in Dooley et al. (2005). They achieved this by using non-deformable wooden blocks with a series of steps, whereas we wished to generate segmented rifts using deformable materials that could be serially sectioned at the end of the model run. Previous models of segmented rifts systems used offset rubber sheets to do this (e.g. McClay et al., 2002; Amilibia et al., 2005). However, these suffered from internal artifacts as the rubber is stretched to generate extension in the overburden it also constricts orthogonal to the extension direction,

resulting in accommodation or transfer zones that are structural lows rather than highs in these locations (e.g. see Sections 2 and 5 of Figure 8 in Amilibia et al., 2005). In order to mitigate these effects we used a hybrid system comprising a single basal stretching sheet, a thin basal silicone detachment and a series of polymer slabs to generate a segmented rift system in the overburden (Figure 2). The stretching rubber sheet generated extension, whilst the basal polymer layer acted as an efficient detachment (during extension and contraction). In contrast, the polymer slabs served to focus extension at these sites, in much the same way that precursor diapirs focus strain in contractional models (e.g. Dooley et al., 2009, 2015; Callot et al., 2007, 2012). Dooley and Schreurs (2012) employed a variety of polymer "crustal weak zones" to focus extension in pull-apart basins and to concentrate and perturb deformation above basement strike-slip zones. Le Calvez and Vendeville (2002), Zwaan et al. (2016) and Zwaan and Schreurs (2017) also used polymer "ridges" to focus or "seed" extensional structures in their models, and Marques et al. (2007) used wedge shaped polymer layers to investigate transform faulting associated with ridge push. Dual motors generated the symmetric extension and contraction in these models (Figure 2).

Models are dynamically scaled such that 1 cm in the model approximates to 1 km in nature (see, for example, Brun et al. 1994 and McClay 1990 for detailed discussions on scaling). Models were conducted with combined horizontal velocities of 1.4×10^{-4} cm/s that yields a strain rate of 1.8×10^{-6} s^{-1}. This rate models an extensional fault system with a moderate displacement rate (e.g. Withjack & Callaway 2000; Dooley et al., 2005). More importantly, post-salt extension was pulsed in order to allow the model salt analog to react to the imposed strain and the differential loads induced by spatially-variable thickness of the synkinematic sediments added after each

139 increment of extension. Models consist of 3 or 4 main evolutionary stages (Table 1): (1) pre-salt
140 extension followed by addition of model salt into the main structural topography addition of a
141 regional salt fringe and thin roof: (2) post-salt extension delivered in a series of pulses, as
142 described above; (3) post-salt loading and downbuilding stage, allowing diapirs that formed in
143 Stage 2 to continue to rise vertically, and; (4) inversion, where the moving endways are detached
144 from the baseplates, the baseplates are clamped in place, and motion is reversed. We focus
145 primarily on the results of one experiment (Model 1, Table 1) in the descriptive sections and use
146 some of the results from two other experiments (Models 2 and 3, Table 1) to discuss salt
147 tectonics styles and salt migration pathways in non-inverted and weakly inverted rifts in the
148 discussion section. The only difference between Model 1 and Models 2 and 3 is that the thin
149 basal detachment layer extended across the entire model base in Model 1, whereas it was limited
150 to just covering the rubber sheet in Models 2 and 3 (see Figure 2).
151
152 *2.2 Modeling Materials*
153
154 As with other physical modeling studies of salt tectonics, we simulated rock salt using ductile
155 silicone and its siliciclastic overburden using brittle, dry, granular material. The silicone was a
156 near-Newtonian viscous polydimethylsiloxane. This polymer has a density of 950 to 980 kg m^{-3}
157 and a dynamic shear viscosity of 2.5×10^4 Pa s at a strain rate of 3×10^{-1} s^{-1} (Weijermars, 1986;
158 Weijermars et al., 1993). In some of our models the salt analog was dyed with minute quantities
159 of powdered pigments in order to track salt flow paths in the completed model. The layered
160 brittle overburden comprised different colored mixtures of silica sand (bulk density of ~1,700 kg
161 m^{-3}; grain size of 300-600 μm; internal friction coefficient, μ, = 0.55–0.65; McClay, 1990;

Krantz, 1991; Schellart, 2000), and hollow ceramic microspheres ("glass beads") having a bulk density of 650 kg m^{-3}, average grain size 90-150 μm, and typical $\mu = 0.45$ (e.g. Rossi and Storti, 2003; Dooley et al., 2009).

The hollows spheres serve to lower bulk grain size, as well as allowing us to modify the density of the brittle overburden. Most physical models of salt tectonics have a layered brittle overburden of pure quartz sand, which creates density ratios that are much higher than those of nature. Exaggerated density ratios erroneously magnify overburden foundering, rise of active diapirs, and expulsion and extrusion of salt (Dooley et al., 2007, 2009). In our models, the pre-rift overburden sediments had a density ratio of equal to that of our model salt by our varying the sand-bead ratio in the brittle section. In this case the ratio of sands to censopsheres in the mixture was equal. This was done to minimize any density- or buoyancy-driven rise of the basal slabs that are also made of the same materials as our salt analog. In Stages 2 and 3 of the model runtime the density of the sedimentary load was increased to 1.1-1.2 times that of our model salt, by increasing the proportion of sands in the mixture to 65%. This was done to encourage salt remobilization from beneath the extensional minibasins in Stage 2 and to keep salt structures (diapirs) growing in Stage 3. Synkinematic strata were added to the model after each 1 cm increment of extension in Stage 2, with aggradation rate governed by any rising diapirs. Similarly, during Stage 3, the height data discussed below governed the regional aggradation rate, to just crest rising diapir networks.

2.3. Data Capture, Visualization, and Interrogation

Computer-controlled cameras photographed the obliquely lit upper surface of the models at set time intervals. A digital image correlation (DIC) system, consisting of a high-resolution stereo charge-coupled device (CCD) system and associated software, tracked the surface-strain history, subsidence, and uplift values, as well as displacement vectors of the top surface of the model. The speckled nature of the sand and cenosphere mixtures used in our models are ideal for this type of monitoring system (see Reber et al., 2020, for further details). Adding synkinematic layers means data is incremental for individual layers during Stages 2 and 3 of Model 1. For more details on DIC monitoring techniques, see Adam et al. (2005). After completion models were impregnated with a gelatin mixture, left to partially dry for 12 hours and then sliced into closely spaced slabs. Coregistered digital photographs of these closely spaced serial sections (≤3.5 mm apart) yielded a 3D voxel of the completed model. Dip sections are the sliced and photographed cross sections, whereas crosslines, arbitrary lines and depth slices are virtual sections constructed from the voxel model. As a result, the crossline, arbitrary line and depth slice images are interpolated and thus not as sharp as those derived directly from photographed dip sections. In addition the 3D salt volume can be extracted from this voxel by coloring the salt in each section with a known pixel value (e.g. white for a value of 255).

3. Experimental Results

3.1 Stage 1: Pre-Salt Extension

Stage 1 comprised 3 cm of uniform extension in order to generate structural topography that was infilled by our salt analog (Table 1). The basal weak slab array shown in Figure 2, was there to

ensure a segmented rift system formed. Height-change data (ΔZ; Figure 3a) generated from our stereo-DIC system reveals the main rift system in Model 1 comprising en-échelon graben that step to the right across the underlying basal slab array (Figure 2). Three main depotroughs are seen along the segmented rift system, separated by zones of higher intra-rift topography, accommodation zones (Figure 3). Strain data illustrate the focused extension along the fault network across the rift system (Figure 3b). On many faults maximum extensional strains, and maximum width of faults, are recorded along their centers, although some deviate from this trend (Figure 3b). Weaker extensional systems form at the margins of the model, far from the central rift system (Figure 3). The accommodation zones are clearly seen in the strain data, and consisted of interlocking arrays of mostly soft linked extension faults with some rotation seen at fault tips (Figure 3b). Between the southern and central and between the central and northern subbasins, clear fault-tip rotation is seen with breaching of the major relay systems separating the subbasins (Figure 3b).

After Stage 1 extension, our salt analog was placed into the three subbasins and allowed to settle (Figure 4a). Once this had settled and filled the structural relief a 12-mm-thick regional layer of our salt analog was emplaced across the model as a series of tiles (Figure 4b), and allowed to degas prior to Stage 2.

3.2 Stage 2: Post-Salt Extension

Our salt analog in Model 1 was buried under a thin (4 mm) sedimentary roof before undergoing a further 6 cm of extension during Stage 2 (Table 1). Figure 5 shows height-change data and strain

231 from Model 1 after applying total of 4 cm of post-salt extension. Synkinematic sediments were
232 added after each 1 cm of basement extension and the values shown in Figure 6 are incremental
233 for that phase of extension, i.e. 3-4 cm post-salt extension. During this period the main
234 depotrough comprised a sigmoidal extensional minibasin located above the original offset graben
235 system (Figure 5a). A series of curvilinear fabrics define relatively minor surface faulting (Figure
236 5a). Strains seen on the upper surface were much more diffuse and spread across the rift system
237 than those seen in the pre-salt extension, Stage 1 (Figure 3). The strain fields formed curvilinear
238 systems of extension that, for the most part, defined minor graben above reactive diapirs, and
239 appear to be diagnostic of detached suprasalt extension (cf. Dooley et al., 2005; Figure 5b).
240 Maximum extensional strains were seen adjacent to the sigmoidal depocenter, as expected,
241 delineating the margins of the main depotrough, and in locations that were accommodation zones
242 during the pre-salt extension phase as the cover collapsed into the developing trough (Figures 3
243 and 5). Minor shortening strains are seen within the extensional minibasin/depotrough due to
244 inner-arc contraction as it subsided into, and expelled, the salt (Figure 5b). The marginal graben
245 at the ends of the model continued to subside during Stage 2 (Figure 5).
246
247 *3.3 Stage 3: Post-Extension Loading*
248
249 Model 1 underwent 9 cm total extension prior to moving on to a downbuilding or post-extension
250 loading phase in Stage 3. Stage 3 lasted for 5 days and synkinematic sediments were added daily,
251 keeping apace and gently covering any positive topography that developed whilst continuing to
252 load negative topography.
253

Height change maps of the model surface of Layers 1 and 4 are shown in Figure 6. Clearly illustrated in Figure 6a are the rising diapir networks as salt was expelled from beneath the composite minibasin in the model center. Comparing Figure 6a to the strain map in Figure 5b one can immediately see that the diapir networks closely conform to the strain patterns seen during Stage 2, evolving from reactive to passive features in Stage 3. Diapirs labelled 1-3 are all located on the footwalls of the main extensional minibasin, and, more importantly, in locations that lie above, and along, what were the original accommodation zones between the original subbasins (see Figures 3, 5 and 6). More linear salt walls are seen rising adjacent to the marginal graben systems and the extensional minibasins is flanked by upwellings along most of its length (Figure 3). Figure 6b illustrates the height change map after 4 days into Stage 3. Activity waned in these systems over time except for the more active and emergent diapirs (1 & 2 in Figure 6b). Smaller amounts of salt rise are seen flanking the central region of subsidence.

3.4 Stage 4: Inversion

In Stage 4 Model 1 was covered with a thin roof sequence and subjected to 25 cm of lateral shortening (Table 1). Height-change maps reveal the evolution of the model during inversion (Figure 7). As expected from previous studies (e.g. Dooley et al., 2009, 2015; Callot et al., 2007, 2012; Duffy et al., 2018), initial shortening resulted in rejuvenation of the two main diapirs formed during Stages 2 and 3 (1 and 2 on Figure 7a). This was followed by uplift of the composite minibasin system and the formation of a series of linear and curvilinear uplifts (Figure 7b). These uplift patterns are very similar to the ridge networks seen during Stage 3 (compare Figures 6a with 7b). With continued shortening the minibasin system continued to rise and salt

277 emerged from Diapir 2 (Figure 7c). The network of curvilinear flanking uplifts continued to rise
278 and become more prominent, and intervening lows shrank in area as they were overthrust (Figure
279 7c). At the end of the experiment Model 1 consisted of a central plateau cored by the inverted
280 minibasin system, and flanked by linear and curvilinear thrust ridges with narrow intervening
281 lows (Figure 7d). Salt sheets emerged from Diapirs 1 and 2 and flowed down into the flanking
282 topographic lows (Figure 7d).
283
284 The final overhead view of Model 1 is shown in Figure 8. In this we see the central uplifted
285 minibasin system forming an oblique plateau across the model, and flanked by the linear and
286 curvilinear faulted ridge network. Flow directions of the salt sheets emanating from Diapirs 1
287 and 2 are indicated by red arrows (Figure 8). Major fault scarps were partially degraded exposing
288 older strata, and some scarps abut, or override scarps with opposite sense of dip (Figure 8). On
289 the right side of the model two fault scarps abut in the south and then coalesce forming a very
290 narrow fault zone (Figure 8). These geometries and relationships are revealed by a series of four
291 sections through Model 1 (Figure 9). The four sections illustrate the decoupled nature of
292 deformation between sub- and suprasalt strata (Figure 9). The main feature is the structurally
293 elevated extensional minibasin system that trended obliquely across the model (Figures 8 and 9).
294 For much of the strike length this feature is flatted topped, and bounded on either side by
295 detached suprasalt thrusts or secondary thrust welds as Diapirs 1 and 2 were squeezed shut
296 (Figures 8 and sections 33 and 55 in Figure 9). Structural elevation of this minibasin system was
297 partly aided by the inversion of subsalt graben that form inversion anticlines in the subsalt strata
298 (Figure 9; see the next section for further discussion). Primary welds denote where the
299 minibasins have touched down on the inverted subsalt strata. Also of interest in the suprasalt

strata are emergent sheets and isolated salt bodies sourced from the squeezed and welded diapirs (e.g. section 33 and 55 in Figure 9), salt-cored thrusts and related secondary welding of portions of these as salt was ejected and hangingwall touched down onto footwall (e.g. Sections 33, 86 and 106, Figure 9). Other structures in the suprasalt section include highly overthrust popdowns, and narrow upright fault zones as hangingwalls collided during shortening (Section 86, Figure 9). A curious structured is observed in many sections, termed an "S" structure due to its shape (see Sections 55 and 86 in Figure 9). We will discuss the origins of this structure in the discussion section. In the subsalt strata structures are very different, consisting of inverted and heavily deformed graben systems in both the center and margins of the model as well as new popup structures (Figure 9).

4. Discussion

In this section we focus on: the formation and location of diapirs during extension and post-extension loading; shortening styles and location in the suprasalt section during inversion; shortening styles and locations in the subsalt section, and; comparison of model results to examples from the High Atlas in Morocco.

4.1 Diapir Formation and Location During Extension

In Model 1 the main diapirs (diapirs 1 and 2, Figure 6), and associated salt wall or ridge networks formed in the footwall of the main extensional systems that flanked the composite extensional minibasin. More specifically the most active diapirs formed in locations spatially

323 associated with the interlocking accommodation zones that originally separated the subbasins
324 (Figures 3, 5 and 6). These locations are similar to those documented in Dooley et al. (2005),
325 although the transfer zones in those models were vertical and rigid. Model 2 was run with almost
326 identical parameters as Model 1, but was not inverted, preserving the diapir geometries and
327 locations (Table 1 and Figure 10). Figure 10a shows the height-change map that evolved during
328 Stage 1 of this model (see Table 1), consisting of an en-échelon series of three graben that run
329 obliquely across the model, similar to that seen in Model 1 (see Figure 3a). The only difference
330 Model 2 showed was the presence of marginal graben that formed closer to the main rift system
331 than that seen in Model 1. This was attributed to the narrower basal silicone detachment used in
332 Model 2 (Figure 2 and Table 1). Likewise, the continued evolution of Model 2 through Stages 2
333 and 3 was very similar to that seen in Model 1 (compare Figures 10b, c with Figures 5a and 6a).
334 The diapir network geometries and most active diapirs in Model 2 were also very similar to those
335 seen in Model 1.
336
337 A section from Model 2 illustrates the extensional minibasins formed above the main graben and
338 diapirs located in the footwalls of these graben (Figure 10d). As we saw in the strain maps for
339 Model 1 there was only minor discrete extension in the suprasalt strata and these are cored by
340 reactive diapirs (Figure 10d). The main diapir in this section is located in the footwall of the
341 main graben system, and just along strike from the accommodation zone that separated the
342 southern and central subbasins (Figure 10a, d). Salt expelled from beneath the subsiding
343 minibasin flowed up onto the footwall and helped feed this growing salt diapir. We believe that
344 salt was also preferentially expelled up and along the accommodation zones that separated the
345 original subbasins and into these growing diapirs, as these accommodation zones have more

346 gentle relief compared to the steep faults that bounded the minibasins, thus offering a more
347 efficient conduit for salt flow.
348
349 In order to corroborate this concept of preferred flow up and along transfer or accommodation
350 zones, images from a third model, Model 3, are shown in Figure 11. Model 3 was subjected to
351 the same amount of extension as Model 1, but a very limited amount of inversion (Table 1). In
352 addition, the lack of a basal detachment across the entirety of the model base meant that
353 shortening in the subsalt section was limited to shortcut thrusts close to the margins of the
354 deformation rig that transferred shortening up to the weaker suprasalt section, with minimal
355 shortening seen in subsalt strata in the central portion of the rift system (Figure 11a-e; Table 1).
356 The lack of deformation in the subsalt strata means that primary welds seen in the sections in
357 Figure 11c-e, occurred during extension rather than during shortening. Depth slices from Model
358 3 illustrate the composite, stepped, minibasin that formed above the en-échelon rift system
359 (Figure 11a-b). The yellow marker salt that initially occupied the central graben of the rift
360 (Figure 11f) is seen to be expelled up and out of this graben system into the footwall, where it
361 helped inflate reactive diapirs that initially formed along these locations (Figure 11a-c; see
362 reactive diapir on the right side Figure 10d for a non-inverted example). Model 3 also had
363 substantial diapirs that flanked the rift in similar positions to those of Models 1 and 2, and yellow
364 marker salt is seen to flow along and up the, now faulted, lower-relief accommodation or transfer
365 zones and into these diapirs (Figure 11d-e). Thus, salt flow during extension and post-
366 extensional loading in Model 3 was multidirectional, being driven by differential loading out and
367 up onto the intra-rift horst blocks both up the main subsalt faults and along lower-relief pathways

such as the transfer zones that separated the subbasins in this rift system. Flow up and along these conduits was eventually curtailed or stopped by primary welding (Figure 11c-e).

4.2 Shortening in the Suprasalt Section

Figure 12 shows the salt volume that was extracted from the serial sections and exported as a point cloud. This image beautifully illustrates the structural style in the shallow section. The central part of the model is dominated by the inverted extensional minibasin system that forms an oblique structural low. Primary thrust welds are denoted by gaps in the data, as the subsalt graben were inverted, welded against the base of the suprasalt strata, and structurally elevated the minibasin system (Figure 12). Note that the position of the primary welds in Model 1 (Figures 9 and 12) differs to those seen in our non-shortened or mildy-shortened Models 2 and 3 (Figures 10 and 11). In Models 2 and 3 the primary welds are located at the minibasin margins where the it welded down onto, or adjacent to, the crest of the footwall block (Figures 10 and 11). In Model 1 primary welds are located more toward the center of the minibasin and are related to the inversion of the subsalt graben system. Any welds that formed at the minibasin margins during Stage 2 extension and Stage 3 downbuilding in Model 1 were sheared off during inversion in a similar fashion to that documented by Roma et al. (2018b). The minibasin system is typically flanked by outward-vergent salt-cored thrusts, secondary thrust welds and remnant high-level salt bodies or sheets (diapirs 1 and 2, Figure 12). Thrust vergence reverses toward the margins of the model, and structures vary from salt-cored thrusts to box-like thrusted folds (Figure 12).

Shortening in the suprasalt section is primarily controlled by the diapir and ridge network that formed during extension and post-extensional loading. This is clearly illustrated in Figure 13, which shows a height-change map, depth slice and dip section from Model 1. The diapir-ridge networks, labelled a-e on Figure 13, localized shortening structures because these are where the overburden was thinnest and thus weakest, and the diapir networks helped to focus deformation. Deformation in the shallow section is clearly detached from the subsalt structures, except where the minibasin system welded onto inverted subsalt graben (Figures 9, 12 and 13c). Height-change maps from the inversion phase also illustrate this reactivation of the pre-inversion diapir-ridge network (compare Figure 7 and 13). Minibasin subsidence patterns in Model 1 were primarily symmetric during extension and post-extensional loading, as evidenced by height-change maps (Figures 5 and 6), and by the stratal geometries seen in cross sections (Figure 9). During inversion the main minibasin system was structurally uplifted by the inverting subsalt graben (Figures 7), with little or no internal deformation except at the minibasin margins where suprasalt thrusts developed (Figures 9 & 13c). Only minor tilting caused by shortening of the main minibasin system is seen in the northern part of the model (section 106, Figure 9). Smaller minibasins developed above the marginal graben systems exhibit more severe tilting as they were carried up in the hangingwalls of major suprasalt thrusts (sections 33 and 55, Figure 9).

As mentioned in Section 3.4, there is a curious structure observed in suprasalt strata in some sections through Model 1 that is termed an “S” structure due to its shape (sections 55 and 86, Figure 9). This structure is found in a deformed salt-cored box fold in the southern part of the model (Figures 9 and 12). A series of sections through this structure give a pseudo-temporal evolution of this structure (Figure 14). The structure started as a faulted box fold, localized along

413 a salt wall (e in Figure 13), that initially formed during extension and post-extension loading.
414 One of the hinges began to fail on one side of this box fold and eventually limb failure occurred,
415 forming a small weld as the core began to narrow (Figure 14a-b). Eventually salt in the core was
416 expelled and the limbs welded, leading to the "S" geometry (Figure 14c).
417
418 *4.3 Shortening in the Subsalt Section*
419
420 We noted briefly in Section 3.4 that deformation in the subsalt strata is very distinct from that
421 seen in suprasalt strata (Figure 9). In subsalt strata the most obvious structures are the popup
422 structures in cross-section views, and none of these are linked to structures in the shallow section
423 (Figure 9). However the most interesting structures are found along the central portions of the
424 model where the pre-salt graben have been strongly deformed and inverted (Figure 9). Some of
425 these structures form the highest subsalt relief seen in Model 1 (e.g. section 33, Figure 9).
426 Height-change maps from Stage 4 of Model 1 clearly illustrate that the main minibasin system
427 was preferentially uplifted as an intact block during shortening (Figure 7). This uplift was thus a
428 result of preferential inversion of the subsalt graben system. This is borne out in cross-section
429 views through Model 1 that clearly show uplift of the main minibasin system as a coherent block
430 forming an almost flat plateau along the length of the center of Model 1 (Figures 7, 8 and 9).
431 Figure 15 shows detailed views of a non-inverted graben from Model 2 and an inverted graben
432 from Model 1. In Model 2 the non-inverted section the structure consists of a mildly asymmetric
433 graben with a smaller keystone graben formed against the more dominant right-side boundary
434 fault (Figure 15a). Figure 15b shows a portion of Section 33 from Model 1 (Figure 9). In it we
435 see a highly inverted basement graben system with a keystone graben system on the right margin

436 as in Model 1 (Figure 15a-b). Inversion of this graben was asymmetric with greater uplift of the
437 left side forming an inversion anticline that structurally elevated the suprasalt minibasin (Figure
438 15b). Based on the geometry of the non-inverted model the right side of the graben also saw
439 significant inversion before being overthrust by a new subsalt thrust (Figure 15b). More minor
440 new thrusts are seen to the left of the graben system. Only a minor amount of structurally-
441 induced tilting is seen in the suprasalt sequence (2.5°, Figure 15b), attributed to the primary weld
442 being slightly off the mid-point of the minibasin. Detached outward-vergent thrusts are located
443 at the minibasin margins (Figure 15b).
444
445 As noted by Amilibia et al. (2005), amongst others, inversion of normal faults in laboratory
446 models using sand is quite limited, sometimes being seen at shallow fault tips but bypass or
447 shortcut faults are far more common. Fault reactivation in nature can occur under stress levels
448 lower than that required to initiate new faults (e.g. Sibson, 1995), due to preexisting faults having
449 a lower cohesive strength and friction coefficient than that of intact rock (Anderson, 1951). The
450 lack of significant reactivation in sandbox models can be explained by the relative lack of
451 difference between the strengths of faulted and unfaulted sands, favoring the formation of new
452 shortcut faults in more favorable orientations (see Amilibia et al., 2005, and Bonini et al., 2011,
453 for more details). Significant reactivation of graben-bounding faults in our models (see Sections
454 33 and 106 in Figure 9; Figure 15b) are attributed to two factors. The first is the presence of the
455 weak basal slabs that initially focused extension. Figure 15a shows remnant 'horns' of the
456 polymer on either side of the graben, and during shortening these would help to focus initial
457 shortening onto the graben system in the central part of the model, much like the way that
458 precursor diapirs focus shortening in purely contractional experiments (e.g. Callot et al., 2007;

459 Dooley et al., 2009, 2015; Duffy et al., 2018). The second, and likely more important, reason is
460 interstitial infiltration of polymer into a narrow zone of the brittle section forming a hybrid
461 rheology along the pre-existing faults. This results in a slight change in color of the granular
462 materials at the sand-silicone interface, which is just visible in Figure 15. Prior to inversion the
463 base and sides of the graben were in contact with silicone, resulting in interstitial infiltration
464 (Figure 15a). The upper portions of the graben-bounding faults were also in contact with silicone
465 again allowing for interstitial infiltration (Figure 15a). During shortening this interstitial
466 infiltration acted as a "lubricant" allowing reactivation and inversion of these faults (Figure 15b).
467 This phenomena of interstitial infiltration has been observed in other laboratories that model salt
468 tectonics with the same materials (O. Ferrer, *pers comm*, 2020), and is likely strongly dependent
469 on the grain size of the strata adjacent to the salt analog. Faults in the granular materials used in
470 physical models are generally dilatant which would enhance this infiltration phenomena.
471
472 *4.4 Comparison to Examples from the Moroccan High Atlas*
473
474 Saura et al. (2014) documented that inversion-related deformation in the central High Atlas of
475 Morocco is mainly focused on minibasin margins with little internal deformation of these
476 minibasins, with diapirs that originally separated these extensional minibasins soaking up much
477 of the deformation, as is seen in our Model 1 (Figure 9). One such example is the Amezraï
478 minibasin (Figure 16a; Saura et al., 2014; Moragas et al., 2017; see location on Figure 1). As in
479 our Model 1, the Amezraï minibasin formed above a basement graben system and was flanked
480 by complex diapirs located in the footwall of this graben system (Figure 16a-b). After inversion
481 these flanks are the sites of significant upturn of flanking strata, thrusts welds and remnant

pedestals, similar to structures found in Model 1 (Figure 16a-b). Similar geometries have just been described from the Maestrat Basin in Spain (Verges et al., 2020). The Azag minibasin lies further to the ENE along the central High Atlas (Figures 1 and 16c; Teixell et al., 2017). Again, this minibasin formed above a basement graben or half-graben system before being it was caught up in Alpine shortening resulting in the welding of adjacent diapirs (thrust or secondary welds; Figure 16c; Teixell et al., 2017), as seen in Model 1. The Azag minibasin also displays significant tilting in the E-W cross section of Figure 16c. Minibasins can tilt during subsidence either before or after welding (Rowan and Weimer, 1998; see Jackson et al., 2019, for more details), but the stratigraphic architecture of the Azag minibasin consists primarily of bowl- and tabular-shaped units indicating relatively symmetric subsidence during minibasin growth. Significant tilting of minibasins caused by shortening is seen in some locations in our Model 1 (Figure 16d), and thus, by analogy, the tilting and welding seen in the Azag minibasin is attributed to Alpine shortening and basement uplift.

One notable difference between our model results (Figures 9 and 16b) and the example sections shown in Figure 16a, c is the amount of deformation seen in the basement or subsalt strata (Figures 9 and 16b). Basement geometries shown in Saura et al. (2014) and Teixell et al. (2017) are inferred due to lack of exposure. The geometry of the basement graben system beneath the Amezraï minibasin shown in Saura et al. (2014) was actually modified by Moragas et al. (2017) based on the results of their physical modeling study. In these natural examples the basement is shown as flat-topped as sub-salt shortening was taken up by simple fault reactivation and vertical uplift of hangingwall blocks (Figure 16a, c). If our physical models are indicative of the deformation intensity one would expect to see in the subsalt basement, then these more pervasive

damage zones could have significant implications for fluid flow and for structural topography at the base of salt. However, our model basement consisted of essentially cohesionless materials, and likely does not accurately represent the strength of basement rocks in the High Atlas or crystalline basement in general. An alternative explanation is that the amount of shortening in Model 1 was simply far more than that experienced in the Central High Atlas. More work is required on this topic. Another topic that requires more study is the geometry of the salt isopach across a basin. In our Model 1 the decoupling between basement and suprasalt strata during both extension and inversion was enhanced by the presence of a salt fringe that covered our entire rift basin. In nature this is unlikely to be the case and many natural examples of syn-rift-salt-bearing basins illustrate the absence of salt across intra-basin horst blocks (e.g. the Scotian margin, Kendell, 2012), or where the salt has variable depositional thickness and influences the degree of coupling between basement and suprasalt strata (e.g. Coleman et al., 2017). The degree of coupling between basement and suprasalt cover is not only dependent on thickness variations of the evaporite sequence but also the composition, or mobility, of the evaporites (e.g. Jackson et al., 2019).

5. Concluding Remarks

Our physical models successfully generated segmented rift systems in a deformable basement that were subsequently infilled with a salt analog and subjected to further extension and finally inversion. During extension and subsequent downbuilding diapir and ridge networks formed that exerted a strong control on deformation styles and patterns during subsequent inversion. Diapir

networks formed primarily in the footwalls of the basement fault system, similar to that described by Dooley et al. (2005) and Moragas et al. (2017). Diapiric growth was encouraged by salt expulsion from beneath the subsiding extensional minibasin systems that formed above the original basement graben, with major diapirs forming consistently in the locations of major relay systems or interlocking transfer zones that originally separated the en-échelon basement graben. These more gently dipping structures facilitated more efficient salt expulsion driving diapiric growth at these locations. Extensional deformation in suprasalt strata was strongly decoupled.

Inversion of these salt-bearing rifts produced strongly decoupled shortening belts in basement and suprasalt sequences. In the suprasalt section deformation geometries and locations were primarily controlled by the salt diapir network produced doing extension and subsequent downbuilding with thrusts formed minibasin margins where the overburden was thinnest and weakest. Extensional minibasins display little or no internal deformation as deformation was soaked up by diapirs and by these marginal thrusts, in a similar fashion to observations from the Central High Atlas of Morocco and other inverted basins. Complex structures form where salt-cored box folds weld shut by hinge and limb failure. In the subsalt section the structural style is very different consisting of strongly inverted and pervasively deformed graben systems along with the formation of new popup structures. Inversion of these graben uplifted and welded the composite extensional minibasin system forming an almost flat-topped plateau across the center of the model. Significant reactivation of graben-bounding faults during inversion was aided by interstitial infiltration of our salt analog that helped “lubricate” the precursor faults.

6. Acknowledgements

This study was funded by the Applied Geodynamics Laboratory consortium consisting of the following companies: Anadarko, BHP Billiton, BP, Chevron, Ecopetrol, EMGS, Eni, ExxonMobil, Fieldwood, Hess, ION Geophysical, Midland Valley, Murphy, Noble Energy, NOOC, Petrobras, Petronas, PGS, Repsol, Rockfield, Talos, Shell, Spectrum Geo, Stone, Talos, TGS, Total, WesternGeco, and Woodside. Additional funding for the authors came from the Jackson School of Geosciences. TD thanks James Donnelly, Nathan Ivivic, Brandon Williamson and Rudy Lucero for logistical support in the modeling laboratories. Nancy Cottington is thanked for colorizing the salt in each dip section from Model 1. The authors thank Jaume Vergés (CSIC, Barcelona) and Grégoire Messager (Equinor, Norway) for initially introducing them to the salt tectonics of the Moroccan High Atlas. Antonio Teixell and Oriol Ferrer are thanked for their kind and thorough reviews of an earlier version of this manuscript. Publication was authorized by the director of the Bureau of Economic Geology, Jackson School of Geosciences, The University of Texas at Austin.

7. References

Adam, J., Urai, J., Wieneke, B., Oncken, O., Pfeiffer, K., and Kukowski, N.: Shear localisation and strain distribution during tectonic faulting - new insights from granular-flow experiments and high-resolution optical image correlation techniques. Journal of Structural Geology, 27(2), 283–301. http://doi.org/10.1016/j.jsg.2004.08.008, 2005.

573

574 Amilibia, A., McClay, K. R., Sabat, F., Muñoz, J. A., and Roca, E.: Analogue modelling of
575 inverted oblique rift systems. Geologica Acta, 3(3), 251–271, 2005.
576

577 Anderson, E.M.: The dynamics of faulting and dyke for- mation with applications to Britain.
578 Olivier and Boyd (eds.). Edinburgh, 203pp., 1951.
579

580 Bonini, M., Sani, F., and Antonielli, B.: Basin inversion and contractional reactivation of
581 inherited normal faults: A review based on previous and new experimental models.
582 Tectonophysics, 522-523(C), 55–88. http://doi.org/10.1016/j.tecto.2011.11.014, 2011.
583

584 Brun, J., Sokoutis, D. and Van Den Driessche, J.: Analogue modelling of detachment fault
585 systems and core complexes. Geology, 22, 319 – 322, 1994.
586

587 Buchanan, J.G., and Buchanan, P.G. (Eds.).: Basin Inversion, Geological Society
588 Special Publication, 88. 596 pp, 1995.
589

590 Buchanan, P.G., and McClay, K.R.: Sandbox experiments of inverted listric and planar
591 fault systems. In: Cobbold, P.R. (Ed.), Experimental and Numerical Modelling of
592 Continental Deformation: Tectonophysics, 188, pp. 97–115, 1991.
593

594 Callot, J. P., Jahani, S., and Letouzey, J.: The role of pre-existing diapirs in fold and thrust belt
595 development. Thrust Belts and Foreland Basins, 309–325, 2007.

596

597 Callot, J. P., Trocme, V., Letouzey, J., Albouy, E., Jahani, S., and Sherkati, S.: Pre-existing salt
598 structures and the folding of the Zagros Mountains. Geological Society London Special
599 Publications, 363(1), 545–561. http://doi.org/10.1144/SP363.27, 2012.

600

601 Coleman, A. J., Jackson, C. A. L., & Duffy, O. B.: Balancing sub- and supra-salt strain in salt-
602 influenced rifts: Implications for extension estimates. Journal of Structural Geology, 102, 208–
603 225. http://doi.org/10.1016/j.jsg.2017.08.006, 2017.

604

605 Couzens-Schultz, B. A., Vendeville, B. C., and Wiltschko, D. V.: Duplex style and triangle zone
606 formation: insights from physical modeling. Journal of Structural Geology, 25(10), 1623–1644.
607 http://doi.org/10.1016/S0191-8141(03)00004-X, 2003.

608

609 Davison, I., Alsop, I., Birch, P., Elders, C., and Evans, N.: Geometry and late-stage structural
610 evolution of Central Graben salt diapirs, North Sea. Marine and Petroleum Geology, 17, 499-
611 522, 2000.

612

613 Dooley, T., McClay, K., Hempton, M., and Smit, D. (2005). Salt tectonics above complex
614 basement extensional fault systems: results from analogue modelling. In: Doré , A. G. & Vining,
615 B. A. (eds) Petroleum Geology: North-West Europe and Global Perspectives—Proceedings of
616 the 6th Petroleum Geology Conference, Geological Society, London, Petroleum Geology
617 Conference Series, 6, 1631-1648, 2005.

618

Dooley, T. P., Jackson, M. P. A., and Hudec, M. R.: Initiation and growth of salt-based thrust belts on passive margins: results from physical models. Basin Research, 19(1), 165–177. http://doi.org/10.1111/j.1365-2117.2007.00317.x, 2007.

Dooley, T. P., Jackson, M. P. A., and Hudec, M. R.: Inflation and deflation of deeply buried salt stocks during lateral shortening. Journal of Structural Geology, 31(6), 582–600. http://doi.org/10.1016/j.jsg.2009.03.013, 2009.

Dooley, T. P., and Schreurs, G.: Analogue modelling of intraplate strike-slip tectonics: A review and new experimental results. Tectonophysics, 574-575, 1–71, 2012.

Dooley, T. P., Jackson, M. P. A., and Hudec, M. R.: Breakout of squeezed stocks: dispersal of roof fragments, source of extrusive salt and interaction with regional thrust faults. Basin Research, 27(1), 3–25. http://doi.org/10.1111/bre.12056, 2015.

Duffy, O. B., Dooley, T. P., Hudec, M. R., Jackson, M. P. A., Fernandez, N., Jackson, C. A.-L., and Soto, J. I.: Structural evolution of salt-influenced fold-and-thrust belts_ A synthesis and new insights from basins containing isolated salt diapirs. Journal of Structural Geology, 114, 206–221. http://doi.org/10.1016/j.jsg.2018.06.024, 2018.

Domènech, M., Teixell, A., & Stockli, D. F.: Magnitude of rift-related burial and orogenic contraction in the Marrakech High Atlas revealed by zircon (U-Th)/He thermochronology and thermal modeling. Tectonics, 35(11), 2609–2635. http://doi.org/10.1002/2016TC004283, 2016.

Durcanin, M. A.: Influence of synrift salt on rift-basin development: Application to the Orpheus Basin, off- shore Canada: M.S. thesis, The State University of New Jersey, 2009.

Ferrer, O., Roca, E., Vendeville, B. C.: The role of salt layers in the hangingwall deformation of kinked-planar extensional faults: Insights from 3D analogue models and comparison with the Parentis Basin. Tectonophysics, 636, 338-350, 2014.

Ferrer, O., McClay, K.R., and Sellier, N. C.: Influence of fault geometries and mechanical anisotropies on the growth and inversion of hangingwall synclinal basins: Insights from sandbox models and natural examples, in C. Child, R. E. Holdsworth, C. A. L. Jackson, T. Manzocchi, J. J. Walsh, and G. Yieldings, eds., The geometry and growth of normal faults: Geological Society of London, Special Publications, 439, doi: 10.1144/ SP439.8., 2016.

Graveleau, F., Malavieille, J., and Dominguez, S.: Experimental modelling of orogenic wedges: A review. Tectonophysics, 538-540(C), 1–66. http://doi.org/10.1016/j.tecto.2012.01.027 , 2012.

Jackson, C. A.-L., & Stewart, S. A.: Composition, Tectonics, and Hydrocarbon Significance of Zechstein Supergroup Salt on the United Kingdom and Norwegian Continental Shelves: A Review. Permo-Triassic Salt Provinces of Europe, North Africa and the Atlantic Margins: Tectonics and Hydrocarbon Potential (pp. 175–201). Elsevier Inc. http://doi.org/10.1016/B978-0-12-809417-4.00009-4, 2017.

Jackson, C. A. L., Duffy, O. B., Fernandez, N., Dooley, T. P., Hudec, M. R., Jackson, M. P. A., and Burg, G.: The stratigraphic record of minibasin subsidence, Precaspian Basin, Kazakhstan. Basin Research, 61(1), 570–25. http://doi.org/10.1111/bre.12393, 2019.

Jackson, C. A. L., Elliott, G. M., Royce Rogers, E., Gawthorpe, R. L., & Aas, T. E. (2019). Salt thickness and composition influence rift structural style, northern North Sea, offshore Norway. Basin Research, 31(3), 514–538. http://doi.org/10.1111/bre.12332, 2019.

Kendell, K. L.: Variations in salt expulsion style within the Sable Canopy Complex, central Scotian margin 1This article is one of a series of papers published in this CJES Special Issue on the theme of Mesozoic–Cenozoic geology of the Scotian Basin. *Canadian Journal of Earth Sciences*, *49*(12), 1504–1522. http://doi.org/10.1139/e2012-069, 2012.

Krantz, R.: Measurements of friction coefficients and cohesion for faulting and fault reactivation in laboratory models using sand and sand mixtures. Tectonophysics, 188, 203-207, 1991.

Krzywiec, P., Mesozoic and Cenozoic evolution of salt structures within the Polish Basin — An overview, Geological Society, London, Special Publications, 363, 381–394, doi: 10.1144/SP363.17, 2012.

Le Calvez, J. H., and Vendeville, B. C.: Experimental designs to model along-strike fault interaction. Journal of the Virtual Explorer, 7, 1–19, 2002.

688 Marques, F., Cobbold, P., and Lourenço, N.: Physical models of rifting and transform faulting,
689 due to ridge push in a wedge-shaped oceanic lithosphere. Tectonophysics, 443, 37–52, 2007.
690
691 Martin-Martin, J. D., Vergés, J., Saura, E., Moragas, M., Messager, G., and Baqués, V.: Diapiric
692 growth within an Early Jurassic rift basin: The Tazoult salt wall (central High Atlas, Morocco),
693 36(1), 2–32. http://doi.org/10.1002/2016TC004300, 2016.
694
695 Michard, A., Ibouh, H., and Charriere, A.: Syncline-topped anticlinal ridges from the high Atlas:
696 a Moroccan conundrum, and inspiring structures from the Syrian arc, Israel. Terra Nova 23, 314-
697 323, 2011.
698
699 McClay, K. R.: Extensional fault systems in sedimentary basins. A review of analogue model
700 studies. Marine and Petroleum Geology, 7, 206–233, 1990.
701
702 McClay, K. R., Dooley, T., Whitehouse, P., and Mills, M.: 4-D evolution of rift systems: Insights
703 from scaled physical models. AAPG Bulletin, 86(6), 935–960, 2002.
704
705 Moragas, M., Vergés, J., Nalpas, T., Saura, E., Martín-Martín, J.-D., Messager, G., and Hunt, D.
706 W.: The impact of syn- and post-extension prograding sedimentation on the development of salt-
707 related rift basins and their inversion: Clues from analogue modelling. Marine and Petroleum
708 Geology, 88, 985–1003. http://doi.org/10.1016/j.marpetgeo.2017.10.001, 2017.
709

Reber, J. E., Cooke, M. L., and Dooley, T. P.: What model material to use? A Review on rock analogs for structural geology and tectonics. Earth-Science Reviews, 202, 103107. http://doi.org/10.1016/j.earscirev.2020.103107, 2020.

Roma, M., Vidal-Royo, O., McClay, K., Ferrer, O., and Muñoz, J.-A.: Tectonic inversion of salt-detached ramp-syncline basins as illustrated by analog modeling and kinematic restoration. Interpretation, 6(1), T127–T144. http://doi.org/10.1190/INT-2017-0073.1, 2017.

Roma, M., Ferrer, O., Roca, E., Pla, O., Escosa, F. O., and Butillé, M.: Formation and inversion of salt-detached ramp-syncline basins. Results from analog modeling and application to the Columbrets Basin (Western Mediterranean). Tectonophysics, 745, 214–228. http://doi.org/10.1016/j.tecto.2018.08.012, 2018a.

Roma, M., Ferrer, O., McClay, K. R., Munoz, J. A., Roca, E., Graticos, O., and Cabello, P.: Weld kinematics of syn-rift salt during basement-involved extension and subsequent inversion: Results from analog models. Geologica Acta, 16(4), 391–410. http://doi.org/10.1344/GeologicaActa2018.16.4.4, 2018b.

Rossi, D., and Storti, F.: New artificial granular materials for analogue laboratory experiments: aluminium and siliceous microspheres. Journal of Structural Geology, 25, 1893–1899, 2003.

Rowan, M., and Weimer, P.: Salt-sediment interaction, northern Green Canyon and Ewing Bank (offshore Louisiana), northern Gulf of Mexico. AAPG Bulletin, 82(5), 1055–1082, 1998.

733

734 Rowan, M. G. and Krzywiec, P.: The Szamotuły salt diapir and Mid-Polish Trough: Decoupling
735 during both Triassic-Jurassic rifting and Alpine inversion. Interpretation, 2(4), SM1–SM18.
736 http://doi.org/10.1190/INT-2014-0028.1, 2014.

737

738 Saura, E., Vergés, J., Martin-Martin, J. D., Messager, G., Moragas, M., and Razin, P.: Syn- to
739 post-rift diapirism and minibasins of the Central High Atlas (Morocco): the changing face of a
740 mountain belt. Journal of the Geological Society, 171(1), 97–105.
741 http://doi.org/10.1144/jgs2013-079, 2014.

742

743 Schellart, W. P. (2000). Shear test results for cohesion and friction coefficients for different
744 granular materials: scaling implications for their usage in analogue modelling. Tectonophysics,
745 324, 1–16, 2000.

746

747 Sibson, R.H.: Selective fault reactivation during basin inversion: potential for fluid
748 redistribution through fault-valve action. In: Buchanan, J.G., Buchanan, P.G. (Eds.),
749 Basin inversion, Geological Society of London Special Publication 88, pp. 3–19. 1995.

750

751 Stewart, S.: Salt tectonics in the North Sea Basin: a structural style template for seismic
752 interpreters. In: Ries, A. C., Butler, R. W. H. & Graham, R. H. (eds). Deformation of the
753 ContinentalCrust: The Legacy of Mike Coward. Geological Society, London, Special
754 Publications, 272, 361-396, 2007.

755

Stewart, S., and Coward, M.: Synthesis of salt tectonics in the southern North Sea, UK. Marine and Petroleum Geology, 12, 457-475, 1995.

Teixell, A., Arboleya, M., Julivert, M., and Charroud, M.: Tectonic shortening and topography in the central High Atlas (Morocco). Tectonics, 22(5), 1051, http://doi.org/10.1029/2002TC001460, 2003.

Teixell, A., Barnolas, A., Rosales, I., and Arboleya, M.-L.: Structural and facies architecture of a diapir-related carbonate minibasin (lower and middle Jurassic, High Atlas, Morocco). Marine and Petroleum Geology, 81, 334–360. http://doi.org/10.1016/j.marpetgeo.2017.01.003, 2017.

Verges, J., Moragas, M., Martín-Martín, J.D., Saura, E., Razin, P., Grelaud, C., Malaval, M., Joussiaume, R., Messager, G., Sharp, I., and Hunt, D.W.: Salt tectonics in the Atlas mountains of Morocco. In: Soto, J.I., Tari, G., Flinch, J. (Eds.), Permo-triassic Salt Provinces of Europe, North Africa and the Atlantic Margins. Tectonics and hydrocarbon potential. 563-576, Elsevier, 2017.

Vergés, J., Poprawski, Y., Almar, Y., Drzewiecki, P. A., Moragas, M., Bover-Arnal, T., Macchiavelli, C., Wright, W., Messager, G., Embry, J-C. and Hunt, D.: Tectono-Sedimentary Evolution of Jurassic-Cretaceous diapiric structures: Miravete anticline, Maestrat Basin, Spain. *Basin Research*, 1–55. http://doi.org/10.1111/bre.12447, 2020.

Weijermars, R.: Polydimethylsiloxane flow defined for experiments in fluid dynamics. Applied Physics Letters, 48(2), 109–111. http://doi.org/10.1063/1.97008, 1986.

779

780 Weijermars, R., Jackson, M. P. A., and Vendeville, B. C.: Rheological and tectonic modeling of
781 salt provinces. Tectonophysics, 217, 143–174, 1993.

782

783 Withjack, M., and Callaway, S.: Active Normal Faulting Beneath a Salt Layer: An Experimental
784 Study of Deformation Patterns in the Cover Sequence. AAPG Bulletin, 84, 627-651, 2000.

785

786 Ziegler, P.A. (Ed.).: Compressional intra-plate deformations in the Alpine Foreland:
787 Tectonophysics, 137. 420 pp, 1987.

788

789 Zwaan, F., Schreurs, G, Naliboff, J., and S. J. H. Buiter, S. J. H.: Insights into the effects of
790 oblique extension on continental rift interaction from 3D analogue and numerical
791 models: Tectonophysics, 693 Part B, 239–260, doi: 10 .1016/j.tecto.2016.02.036, 2016.

792

793 Zwaan, F., and Schreurs, G. (2017). How oblique extension and structural inheritance influence
794 rift segment interaction: Insights from 4D analog models. Interpretation, 5(1), SD119–SD138.
795 http://doi.org/10.1190/INT-2016-0063.1, 2017.

796

797

Figure Captions

Figure 1. Summary geological map of the central High Atlas of Morocco. Jurassic intrusive massifs containing upper Triassic shale, basalt and evaporite inliers have been interpreted as former diapiric ridge that separated extensional minibasins formed during Permian to Early Jurassic punctuated rifting. AmMB, Amezraï minibasin. AzMB, Azag minibasin. Map redrawn and modified from Teixell et al., 2017.

Figure 2. Summary of experimental setup used in models shown in this study. (a) Cross section view of the pre-rift setup. Models consist of a stretching rubber sheet overlain by a thin basal detachment and polymer 'slabs' covered by a layered sandpack. (b) Overhead view of deformation rig prior to emplacement of the layered pre-rift overburden. See text for further details.

Figure 3. (a) Height-change map of Model 1 after pre-salt extension. Three en-échelon graben in model center are separated by accommodation zones with relays. Marginal graben formed at the model periphery. (b) Strain map of Model 1 during pre-salt extension. Accommodation zones consist of interlocking extensional faults. Note that some relays are breached. See text for further details.

Figure 4. Emplacement of syn-rift salt in Model 1. (a) Pre-salt graben are infilled with our salt analog. Colored silicone was emplaced in the central graben system in order to track flow in the final cross-section views. (b) A regional salt fringe is then emplaced across the entire model.

Figure 5. (a) Height-change map during post-salt extension in Model 1. Post-salt extension was now 4 cm. Note the composite minibasin extending across the model center, above the original graben system. (b) Strain map of the same increment of post-salt extension. Note the diffuse strains in the suprasalt cover. Most extensional strains mark outer-arc extension above reactive diapirs. Note the minor shortening strains within the minibasin due to inner-arc contraction within the subsiding minibasin.

Figure 6. Height-change maps of Model 1 after 16 (a) and 48 (b) hours of post-extension loading. In (a) we see the major diapir networks, formed during extension, continuing to rise as salt is expelled from beneath adjacent minibasins. After 48h loading (b) activity is now focused on two major diapirs. See main text for more details.

Figure 7. Height-change maps (a-d) reveal the evolution of Model 1 during inversion. Initial shortening and uplift was focused on the diapirs formed during extension and loading (a), followed by uplift of the composite minibasin above the model center and rejuvenation of the diapir and ridge networks (b-d).

Figure 8. Overhead view of Model 1 after 25 cm shortening. Diapirs 1 and 2 are clearly visible in this view as emergent salt sheets. Section lines are those shown in Figure 9. See text for further details.

843 Figure 9. Representative sections through Model 1. Locations are shown on Figure 8. Inset
844 shows the model stratigraphy.
845
846 Figure 10. Details from Model 2 (see Table 1). (a) Height-change map that evolved during Stage
847 1 of Model 2. (b) Height-change map of Model 2 during post-salt extension. (c) Height-change
848 map of Model 2 during post-extension loading. (d) Cross section from Model 2 illustrating
849 extensional minibasins and diapirs of varying heights formed in the footwalls of the subsalt
850 graben. See text for further details.
851
852 Figure 11. Details of Model 3. (a-b) Depth slices through Model 3. (c-e) Arbitrary lines through
853 a portion of Model 3. (f) Original location of yellow marker 'salt' in the central graben of Model
854 3. See text for further details.
855
856 Figure 12. 3D reconstruction of the salt volume from Model 1. See main text for details.
857
858 Figure 13. (a) Height-change map from Stage 3 of Model 1 illustrating the diapir and ridge
859 networks that formed during extension rising during post-extension loading. (b-c) Depth slice
860 and dip section through Model 1 illustrating the five (a-e) main diapir networks.
861
862 Figure 14. Detailed views (a-c) of sections through Model 1 illustrating the evolution of an "S"
863 structure.
864

Figure 15. (a) Detailed view of a non-inverted subsalt graben from Model 2. Note the asymmetric geometry and the formation of a keystone structure. (b) Detailed view of an inverted subsalt graben from Model 1. Inversion of this graben uplifted and welded the overlying extensional minibasin.

Figure 16. (a) Cross section through the Amezraï minibasin, Moroccan High Atlas. Note the uptilted minibasin margins, lack of internal deformation within the minibasin and the complex flanking diapirs and thrust welds. Redrawn from Moragas et al. (2017). (b) Detailed views of minibasin margins and associated secondary thrust welds from Model 1. (c) E-W cross section through the Azag minibasin. Note the thrust welds and tilted nature of the minibasin. Redrawn from Teixell et al. (2017). (d) Detail of a section from Model 1 illustrating a tilted minibasin, primary weld on top of an inverted subsalt graben, and secondary thrust welds on either side of the minibasin.

Table 1. Model names and values for extension and inversion for experiments described in the main text. *denotes basal detachment was limited to the central region of the model.

Model Name	Basal detachment thickness (cm)	Number of basal slabs and their height (cm)	Regional salt fringe thickness (cm)	Pre-salt Extension (cm)	Post-salt extension (cm)	Total extension (cm)	Inversion (cm)
				Stage 1	Stages 2-3		Stage 4
Model 1	0.4	3 x 1.5	1.2	3	6	9	25
Model 2	0.4*	3 x 1.5	1.2	3	6	9	0
Model 3	0.4*	3 x 1.5	1.2	2.5	6.5	9	8

Table 1. Model names and values for extension and inversion for experiments described in the main text. *denotes basal detachment was limited to the central region of the model.

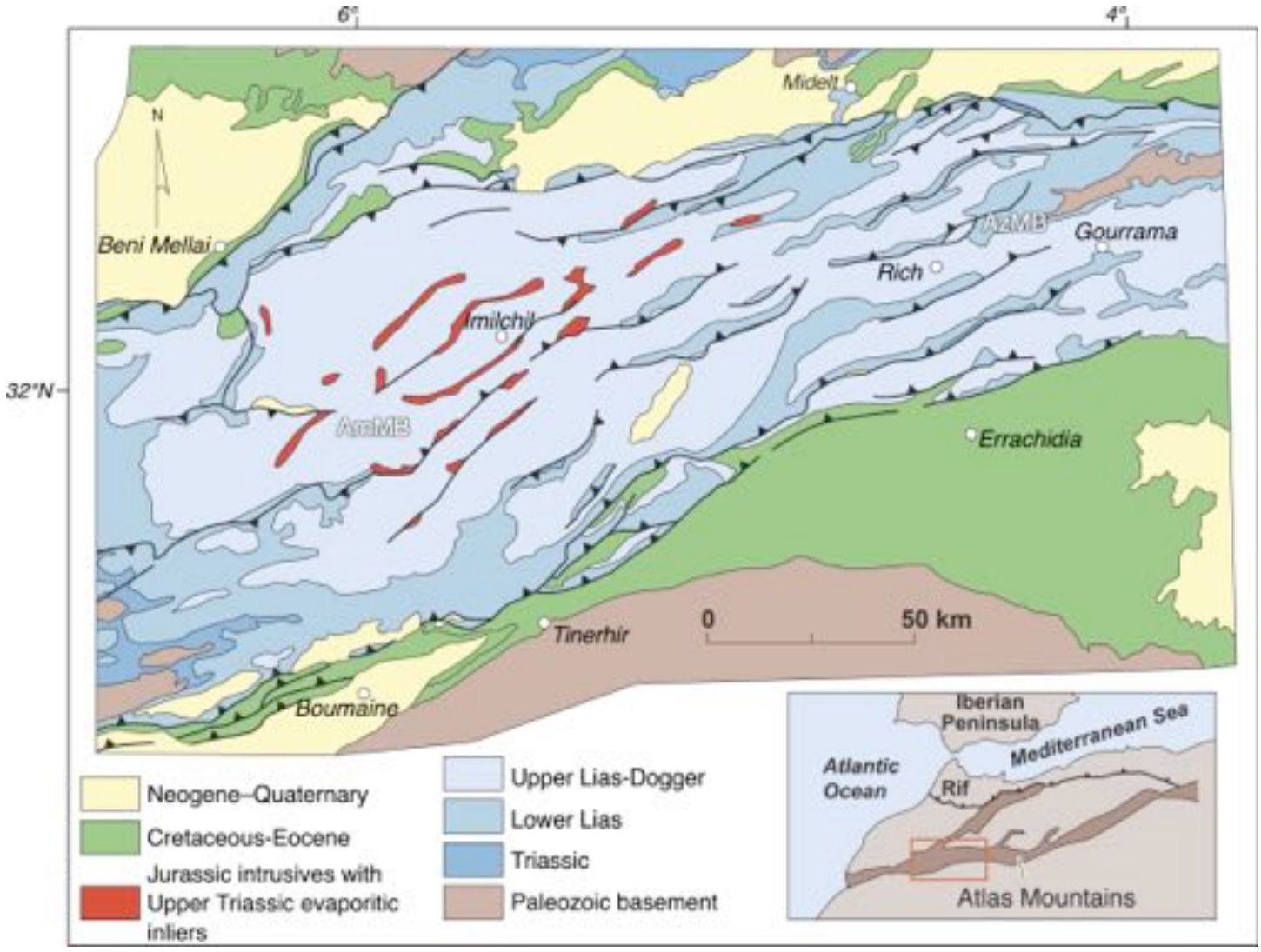
6°
4°
32°N
N
Midelt
Beni Mellai
HAZMB
Gourrama
Rich
Imilchil
AtlMB
Errachidia
Tinerhir
0
50 km
Boumaine
Neogene–Quaternary
Cretaceous-Eocene
Jurassic intrusives with Upper Triassic evaporitic inliers
Upper Lias-Dogger
Lower Lias
Triassic
Paleozoic basement
Iberian Peninsula
Mediterranean Sea
Atlantic Ocean
Rif
Atlas Mountains

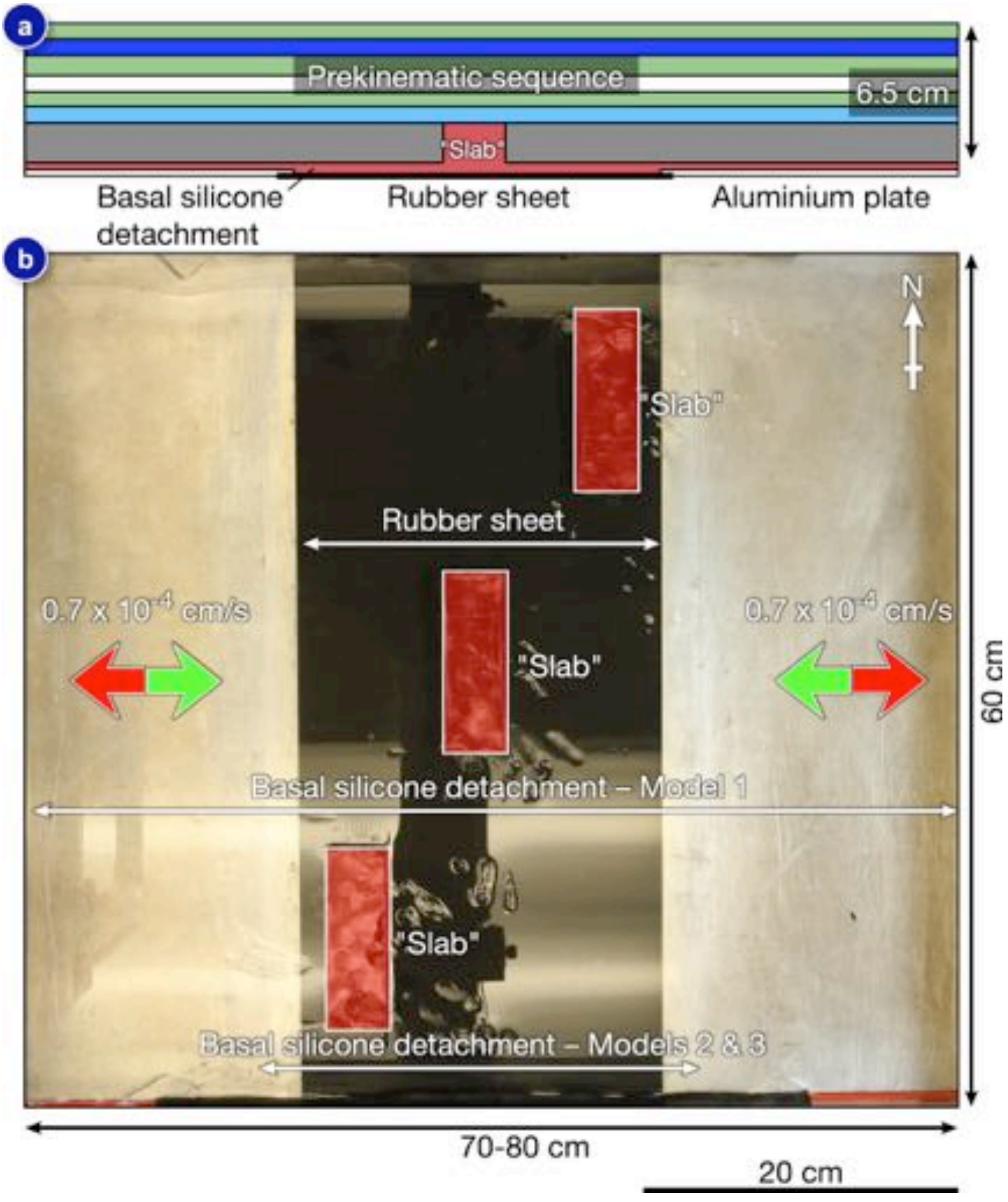
a
Prekinematic sequence
6.5 cm
"Slab"
Basal silicone detachment
Rubber sheet
Aluminium plate
b
N
"Slab"
Rubber sheet
0.7 x 10-4 cm/s
0.7 x 10-4 cm/s
"Slab"
Basal silicone detachment – Model 1
"Slab"
Basal silicone detachment – Models 2 & 3
60 cm
70-80 cm
20 cm

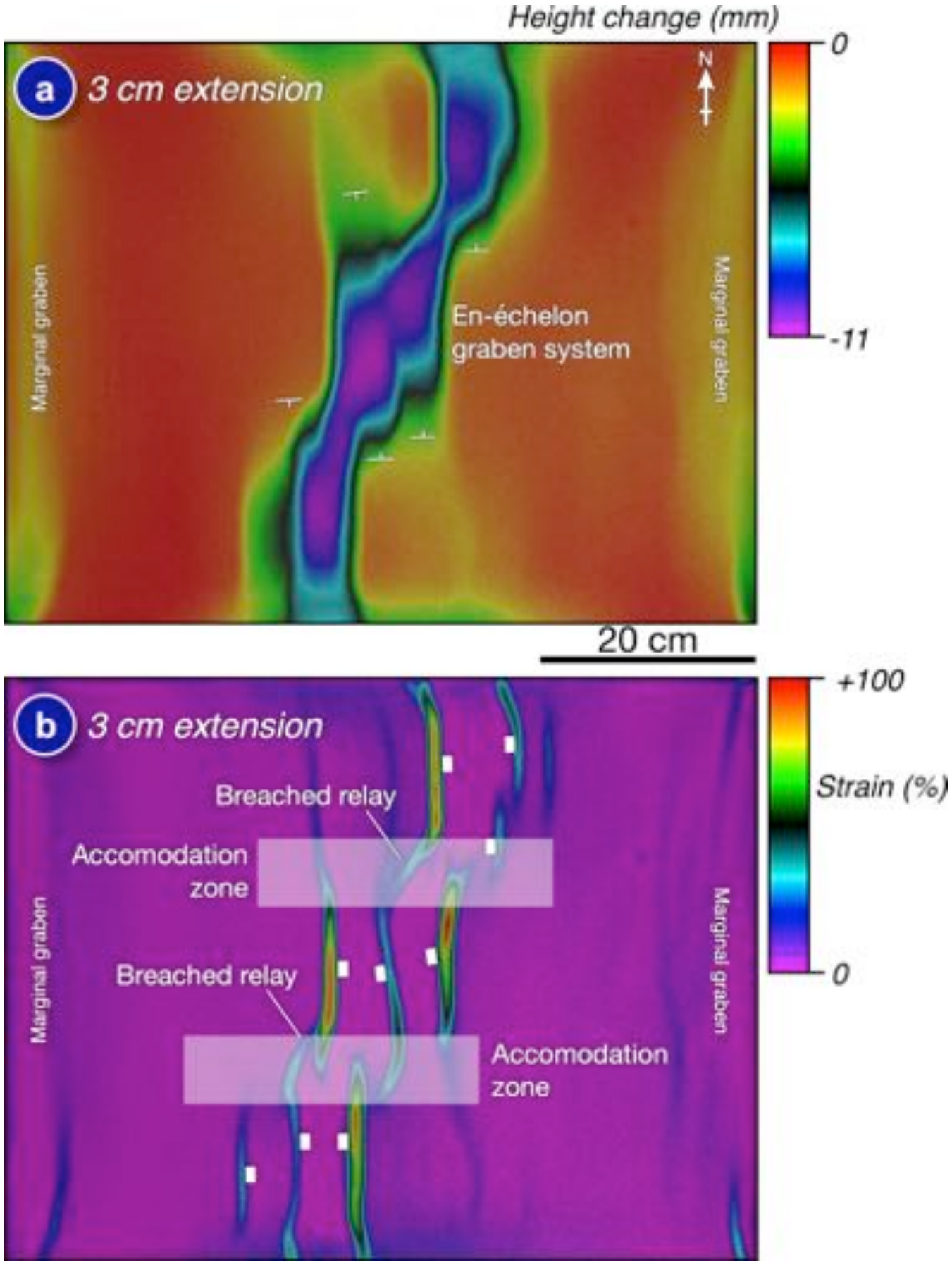
Height change (mm)
0
-11
a
3 cm extension
N
Marginal graben
Marginal graben
En-échelon
graben system
20 cm
b
3 cm extension
+100
Strain (%)
0
Breached relay
Accomodation
zone
Breached relay
Accomodation
zone
Marginal graben
Marginal graben

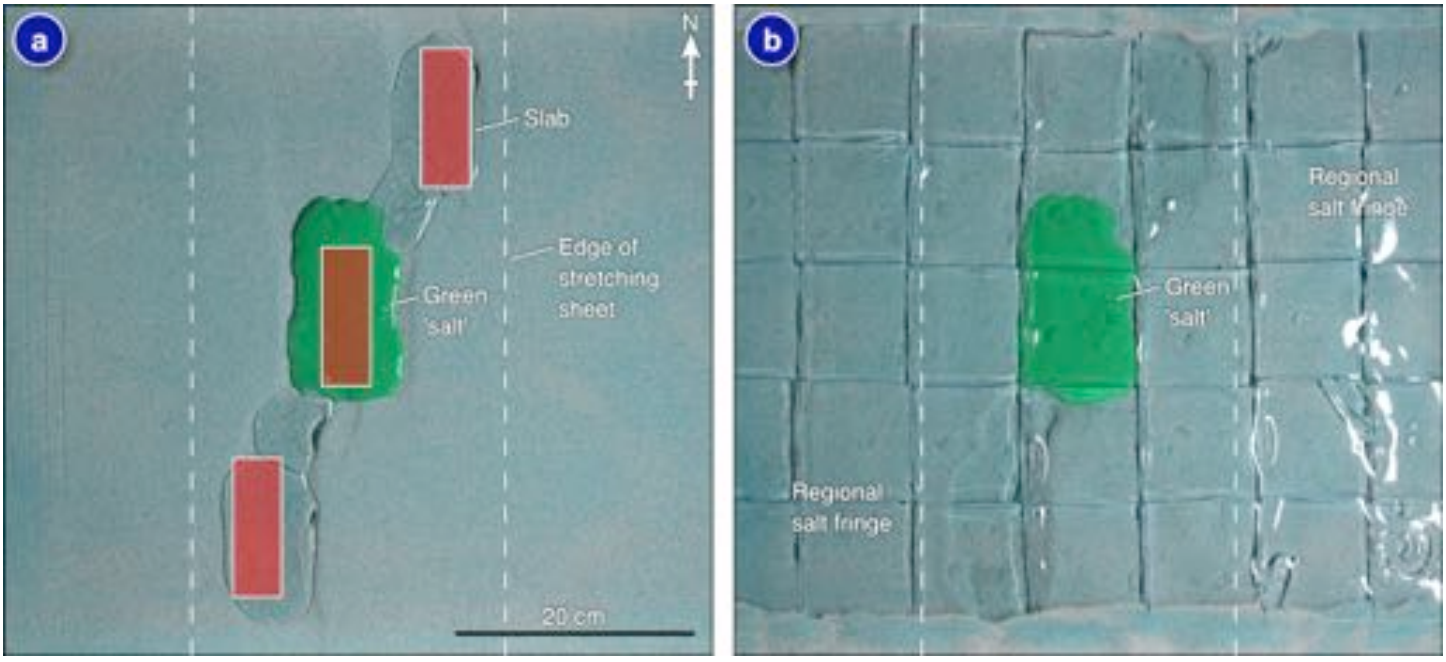
a
N
Slab
Edge of
stretching
sheet
Green
'salt'
20 cm
b
Regional
salt fringe
Green
'salt'
Regional
salt fringe

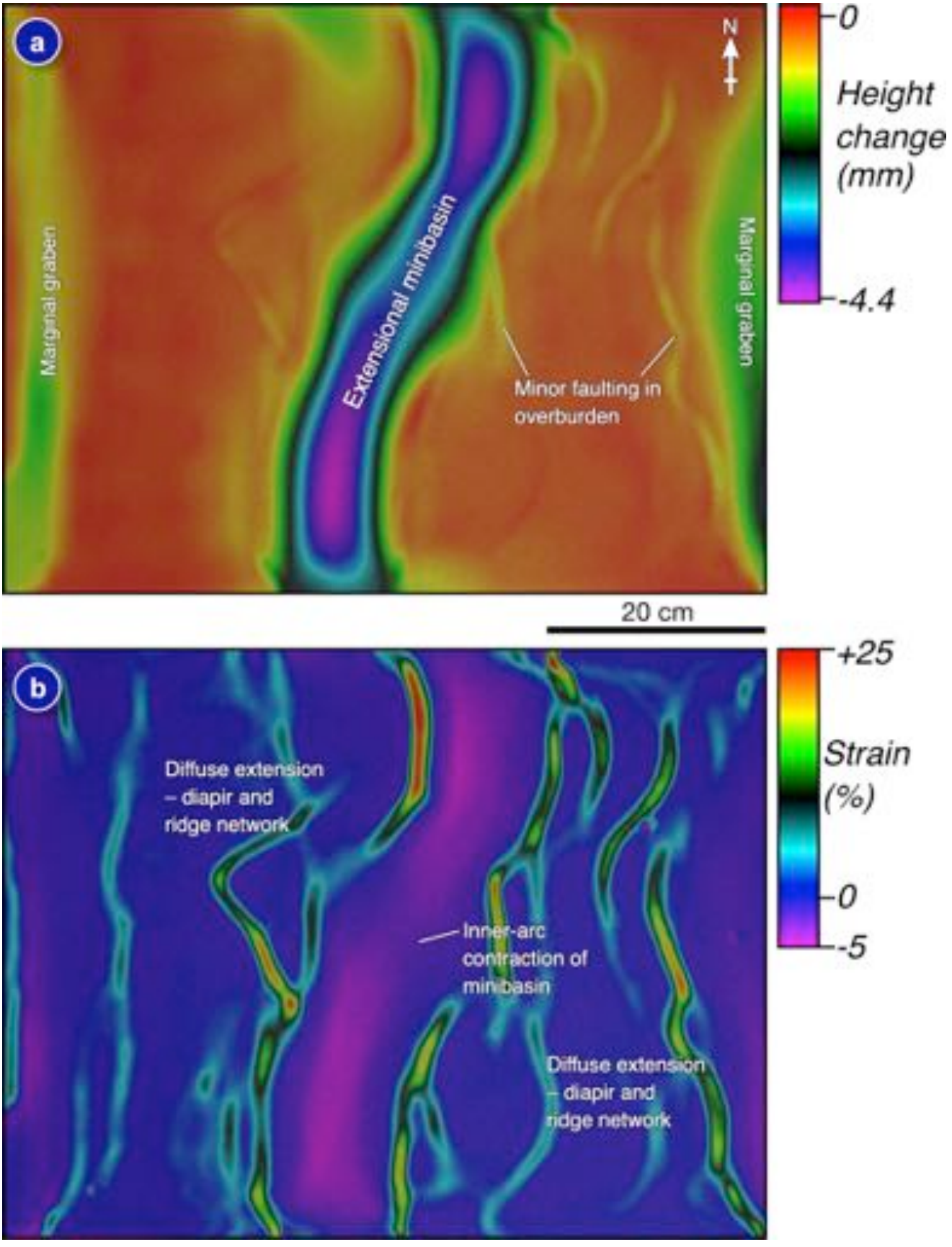
a
N
Marginal graben
Extensional minibasin
Minor faulting in overburden
Marginal graben
0
Height change (mm)
-4.4
20 cm
b
Diffuse extension – diapir and ridge network
Inner-arc contraction of minibasin
Diffuse extension – diapir and ridge network
+25
Strain (%)
0
-5

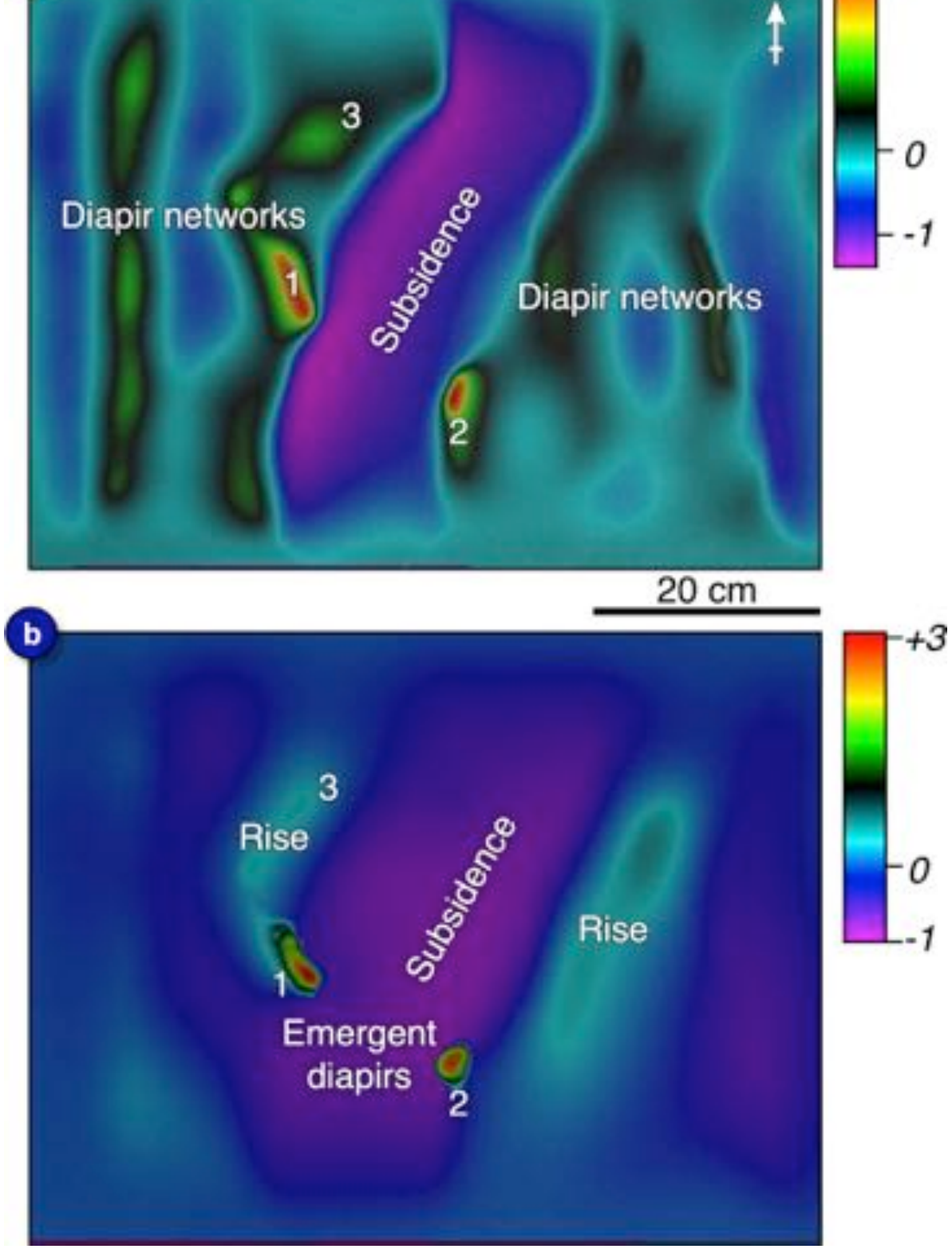
a
Height change (mm)
+2
0
-1
N
3
Diapir networks
1
Subsidence
Diapir networks
2
20 cm
b
+3
0
-1
3
Rise
Subsidence
Rise
1
Emergent
diapirs
2

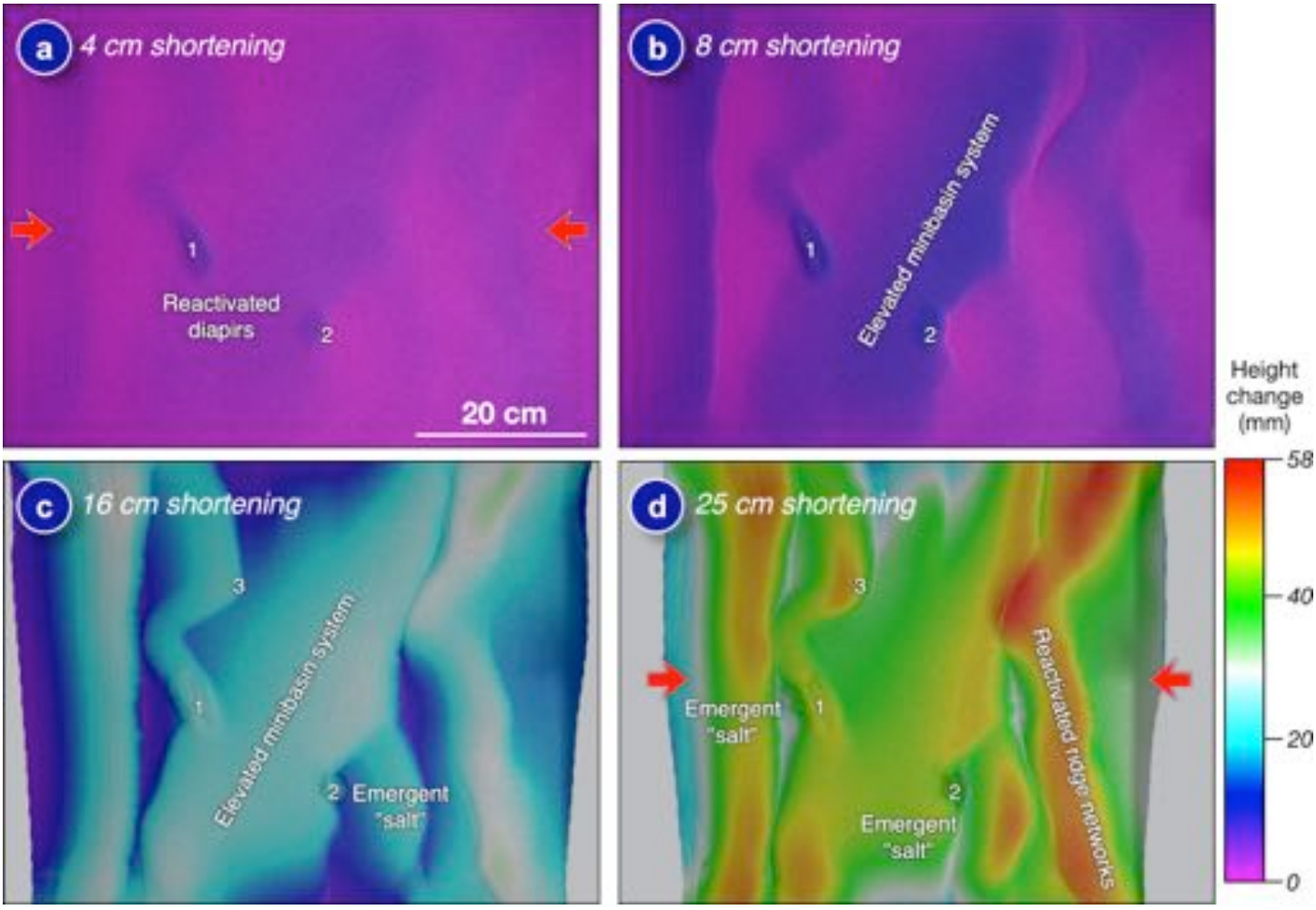
a
4 cm shortening
1
Reactivated
diapirs
2
20 cm
b
8 cm shortening
Elevated minibasin system
1
2
Height
change
(mm)
58
40
20
0
c
16 cm shortening
3
Elevated minibasin system
1
2 Emergent
"salt"
d
25 cm shortening
3
Emergent
"salt"
1
Reactivated ridge networks
2
Emergent
"salt"

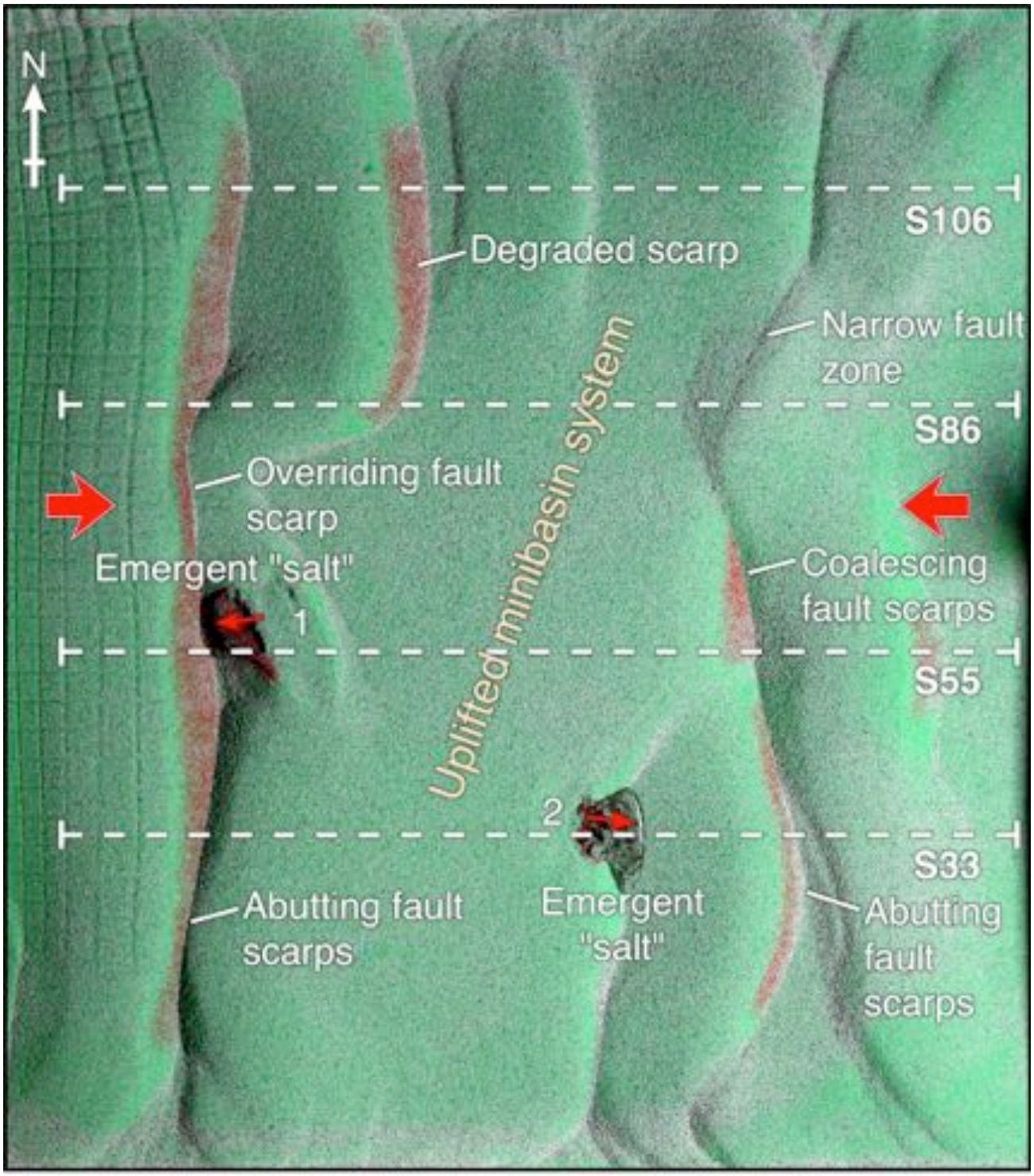
N
S106
Degraded scarp
Narrow fault zone
S86
Overriding fault scarp
Emergent "salt"
1
Uplifted minibasin system
Coalescing fault scarps
S55
2
S33
Abutting fault scarps
Emergent "salt"
Abutting fault scarps
20 cm

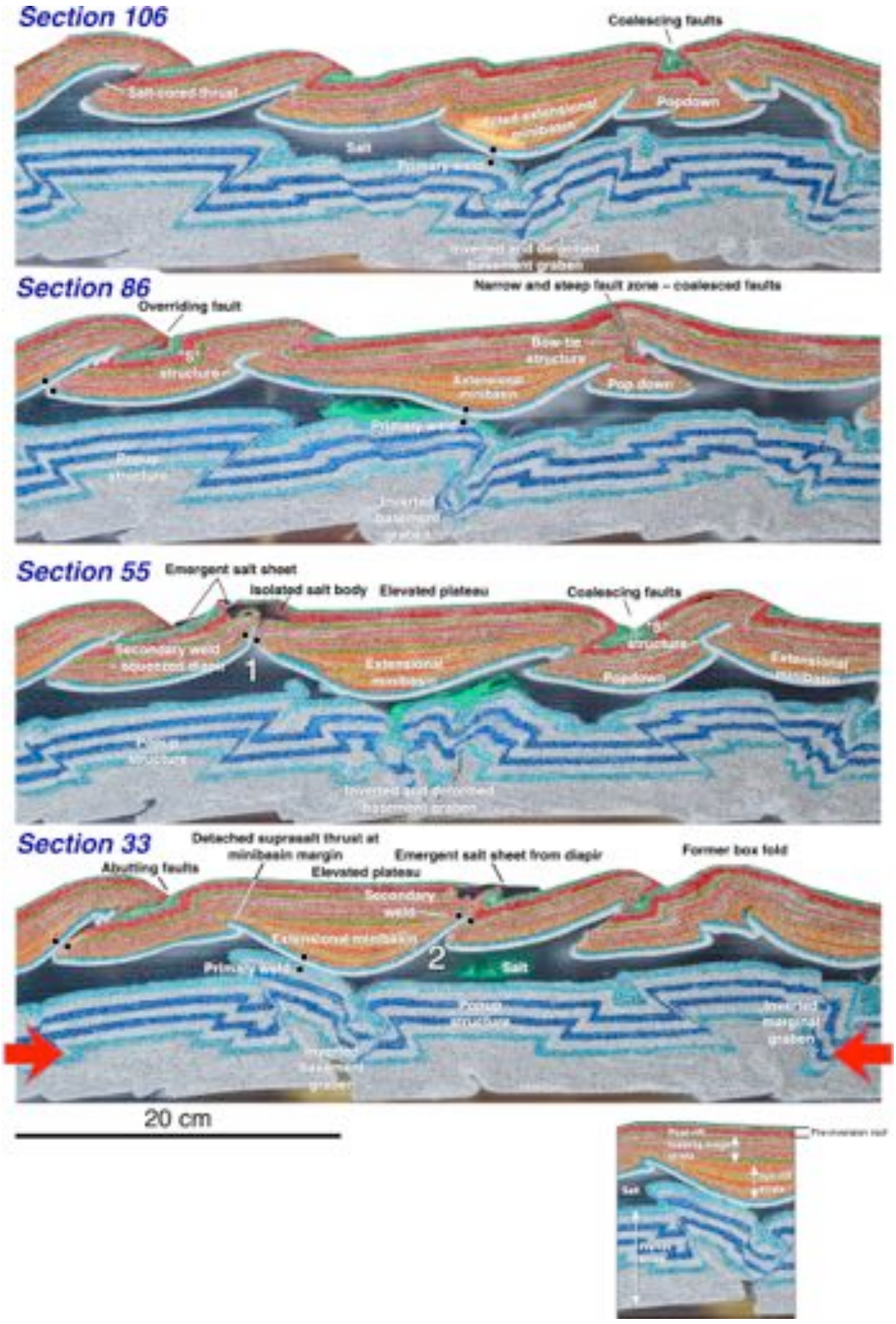
Section 106
Coalescing faults
Salt-cored thrust
Salt
Popdown
Section 86
Narrow and steep fault zone – coalesced faults
Overriding fault
Bow-tie structure
Pop down
Section 55
Emergent salt sheet
Isolated salt body
Elevated plateau
Coalescing faults
Secondary weld
Extensional minibasin
Popdown
1
Section 33
Detached supresalt thrust at minibasin margin
Former box fold
Abutting faults
Elevated plateau
Emergent salt sheet from diapir
Secondary weld
Extensional minibasin
2
Salt
20 cm

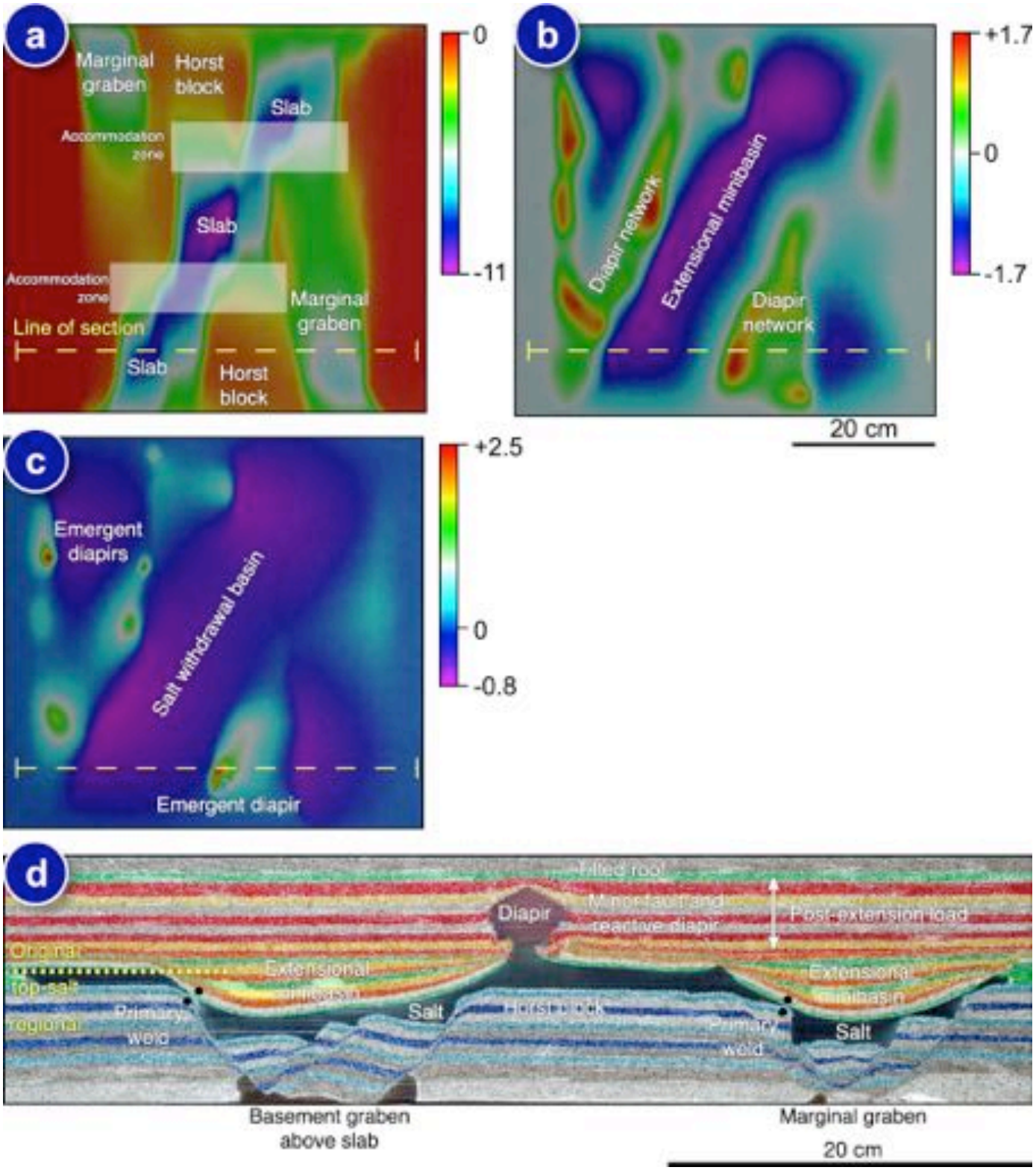
a
Marginal graben
Horst block
Slab
Accommodation zone
Slab
Accommodation zone
Marginal graben
Line of section
Slab
Horst block
0
-11
b
Diapir network
Extensional minibasin
Diapir network
+1.7
0
-1.7
20 cm
c
Emergent diapirs
Salt withdrawal basin
Emergent diapir
+2.5
0
-0.8
d
Diapir
Post-extension load
Extensional
Salt
Primary weld
Salt
Basement graben above slab
Marginal graben
20 cm

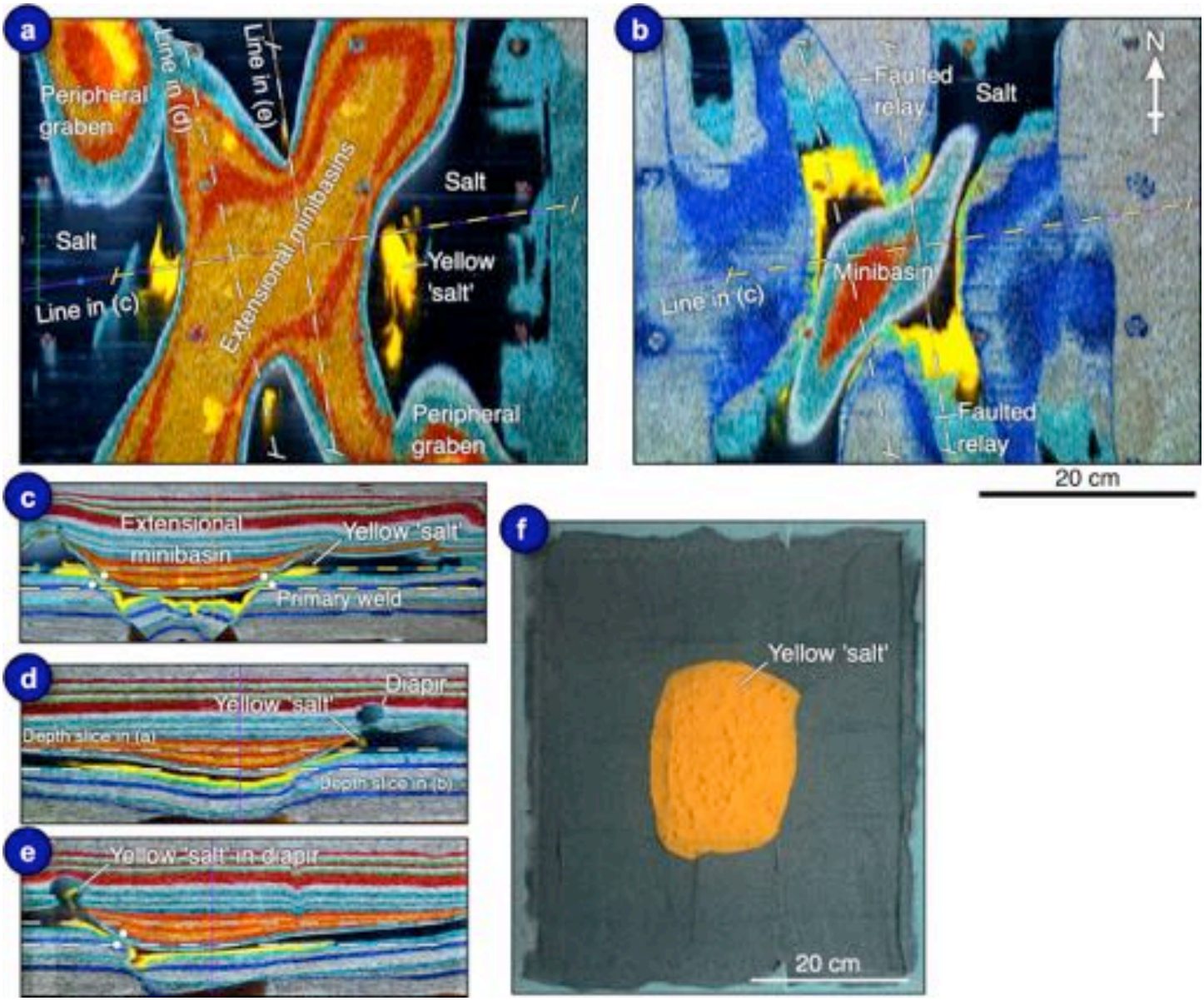
a
Peripheral graben
Line in (d)
Line in (e)
Salt
Salt
Yellow 'salt'
Line in (c)
Extensional minibasins
Peripheral graben
b
Faulted relay
Salt
N
Minibasin
Line in (c)
Faulted relay
20 cm
c
Extensional minibasin
Yellow 'salt'
Primary weld
d
Diapir
Yellow 'salt'
Depth slice in (a)
Depth slice in (b)
e
Yellow 'salt' in diapir
f
Yellow 'salt'
20 cm

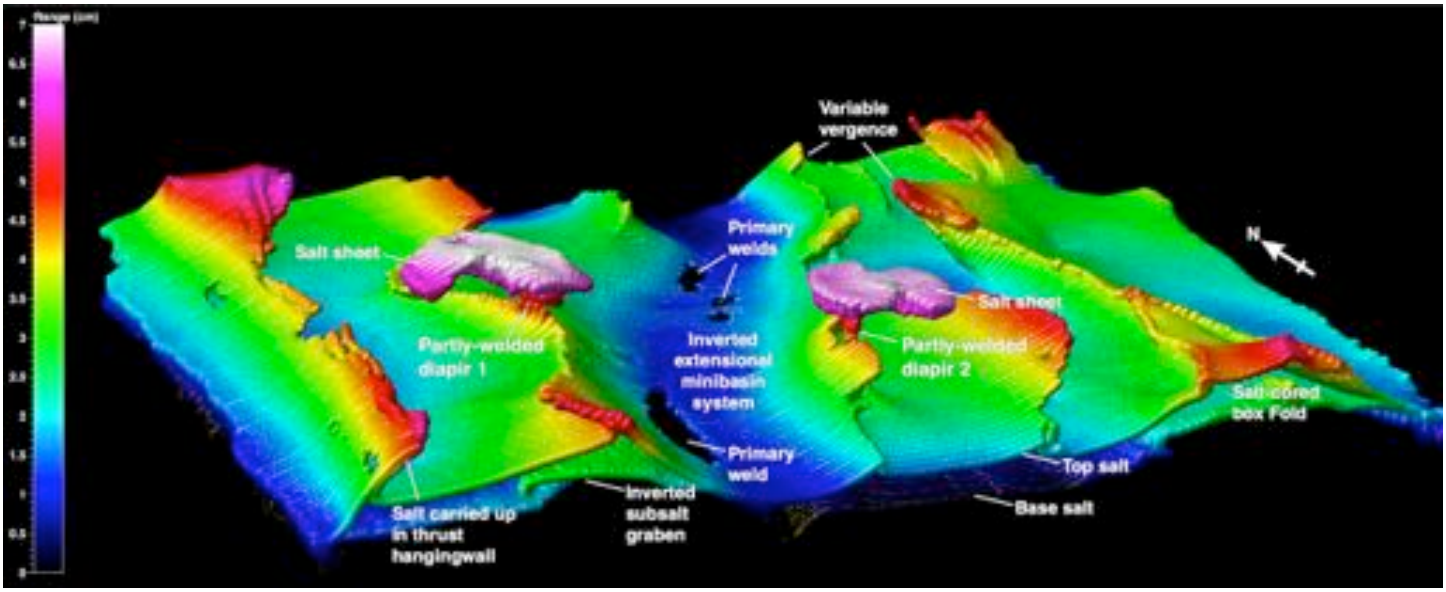
Variable vergence
Primary welds
Salt sheet
Partly-welded diapir 1
Inverted extensional minibasin system
Salt sheet
Partly-welded diapir 2
Salt cored box Fold
Primary weld
Top salt
Inverted subsalt graben
Base salt
Salt carried up in thrust hangingwall
N

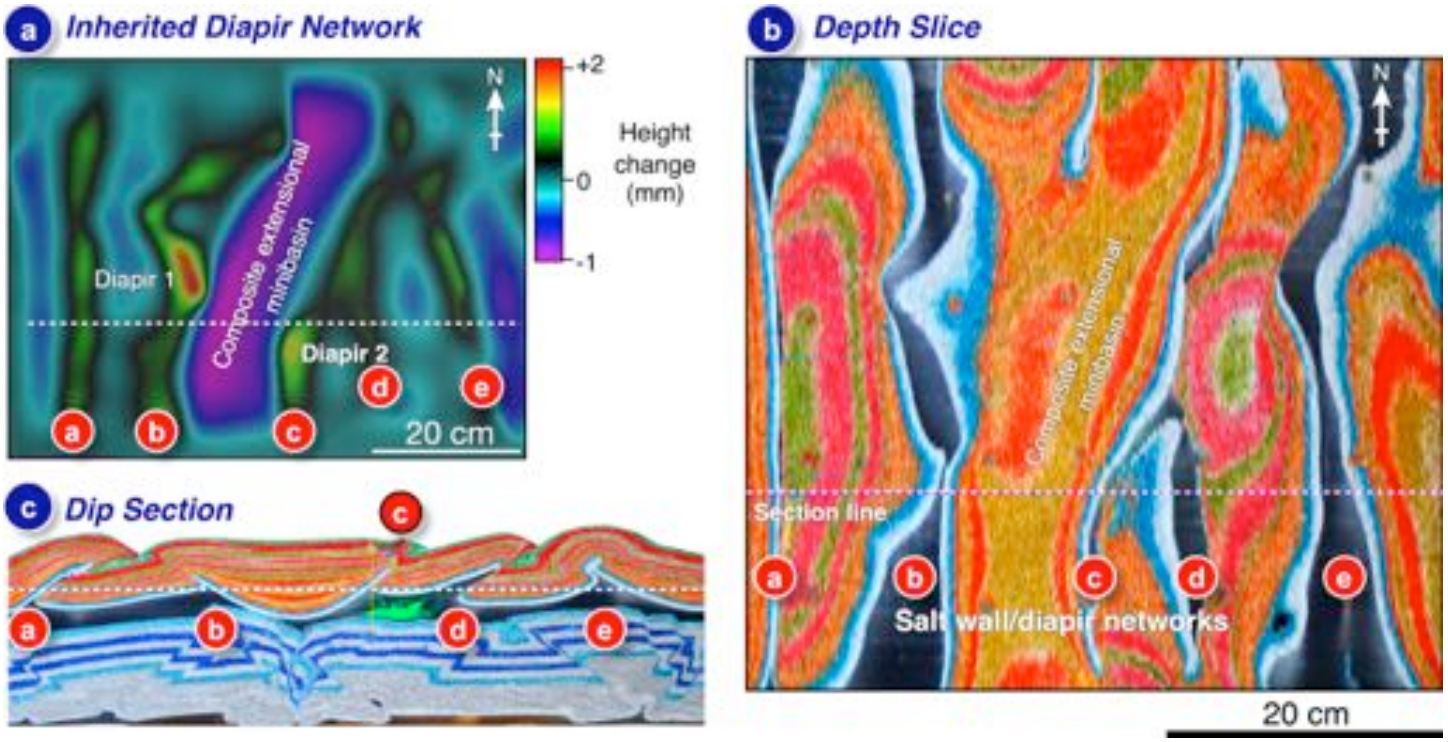
a Inherited Diapir Network
N
+2
0
-1
Height change (mm)
Diapir 1
Composite extensional minibasin
Diapir 2
a
b
c
d
e
20 cm
b Depth Slice
N
Composite extensional minibasin
Section line
a
b
c
d
e
Salt wall/diapir networks
20 cm
c Dip Section
c
a
b
d
e

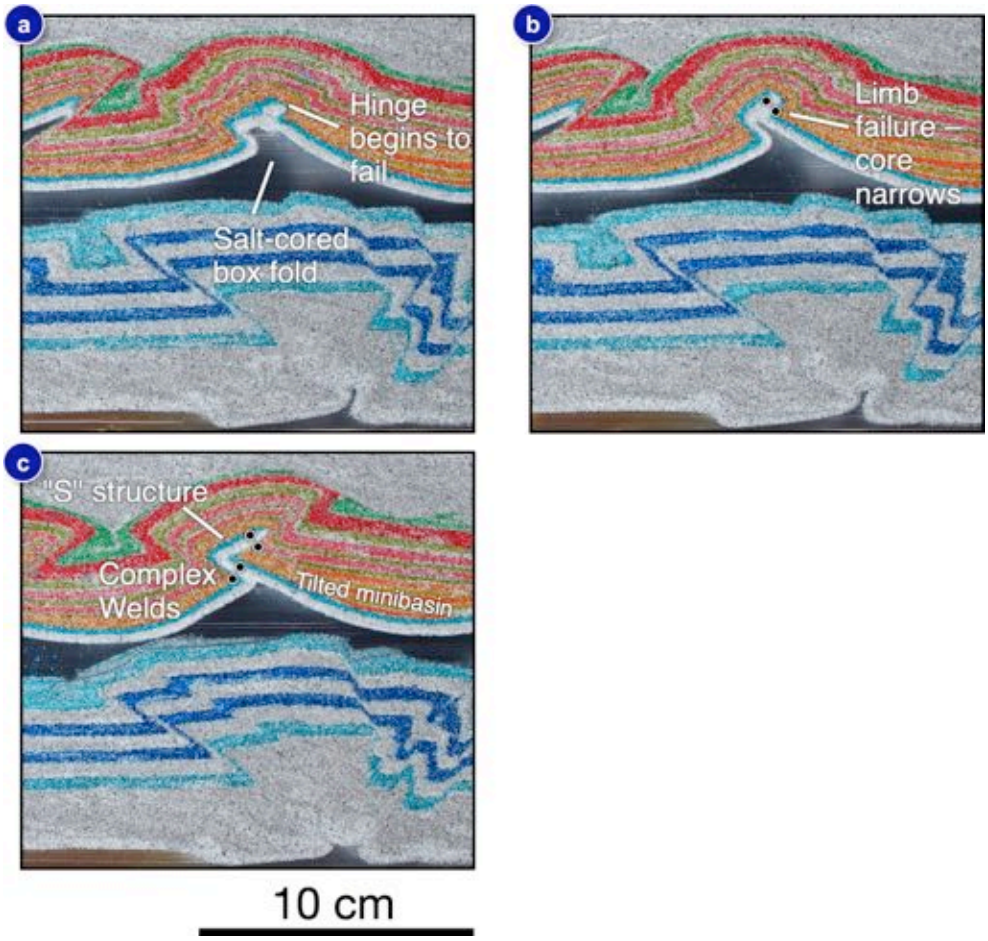
a
Hinge
begins to
fail
Salt-cored
box fold
b
Limb
failure
core
narrows
c
"S" structure
Complex
Welds
Tilted minibasin
10 cm

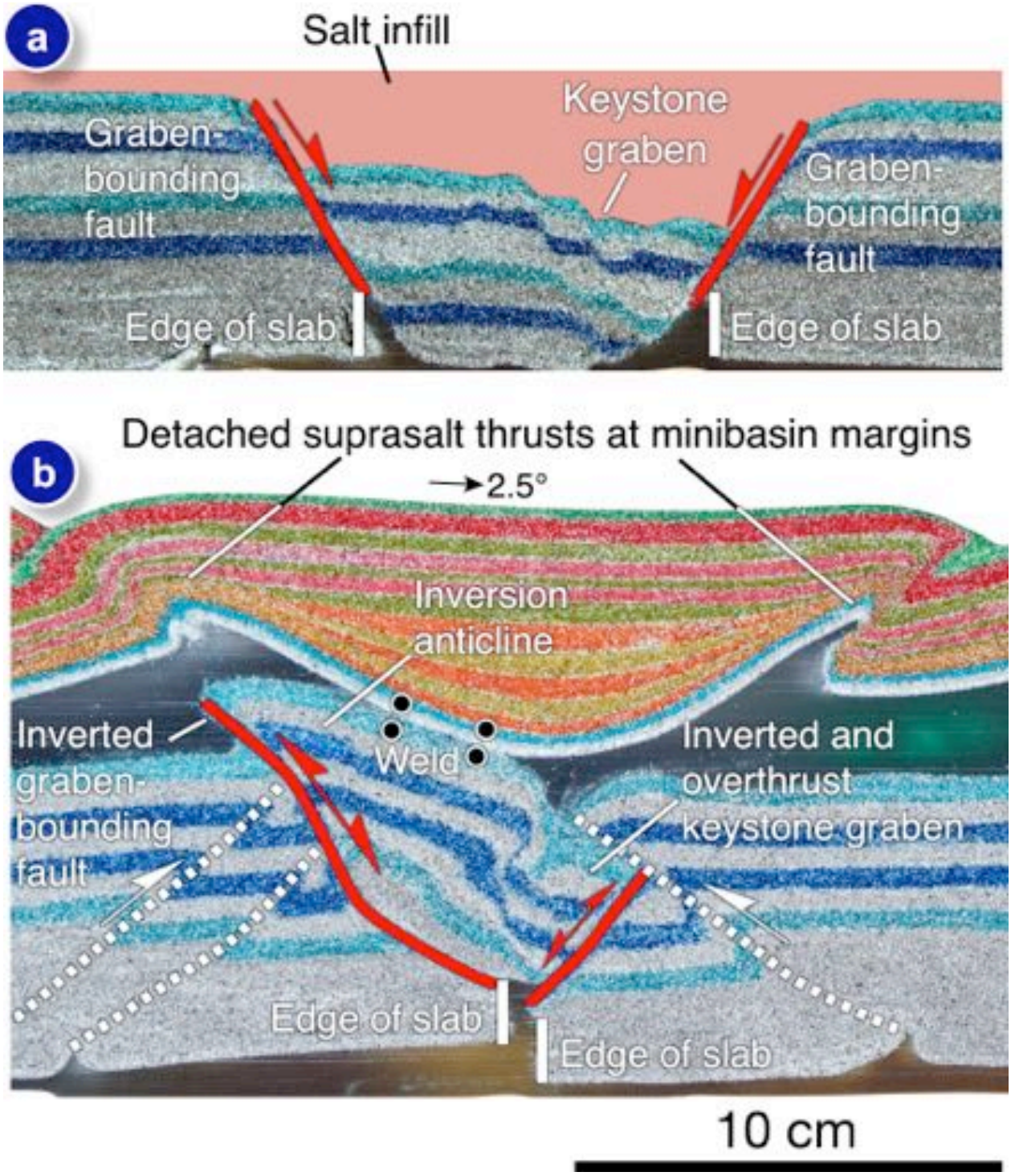
a
Salt infill
Keystone graben
Graben-bounding fault
Graben-bounding fault
Edge of slab
Edge of slab
b
Detached suprasalt thrusts at minibasin margins
2.5°
Inversion anticline
Weld
Inverted graben-bounding fault
Inverted and overthrust keystone graben
Edge of slab
Edge of slab
10 cm

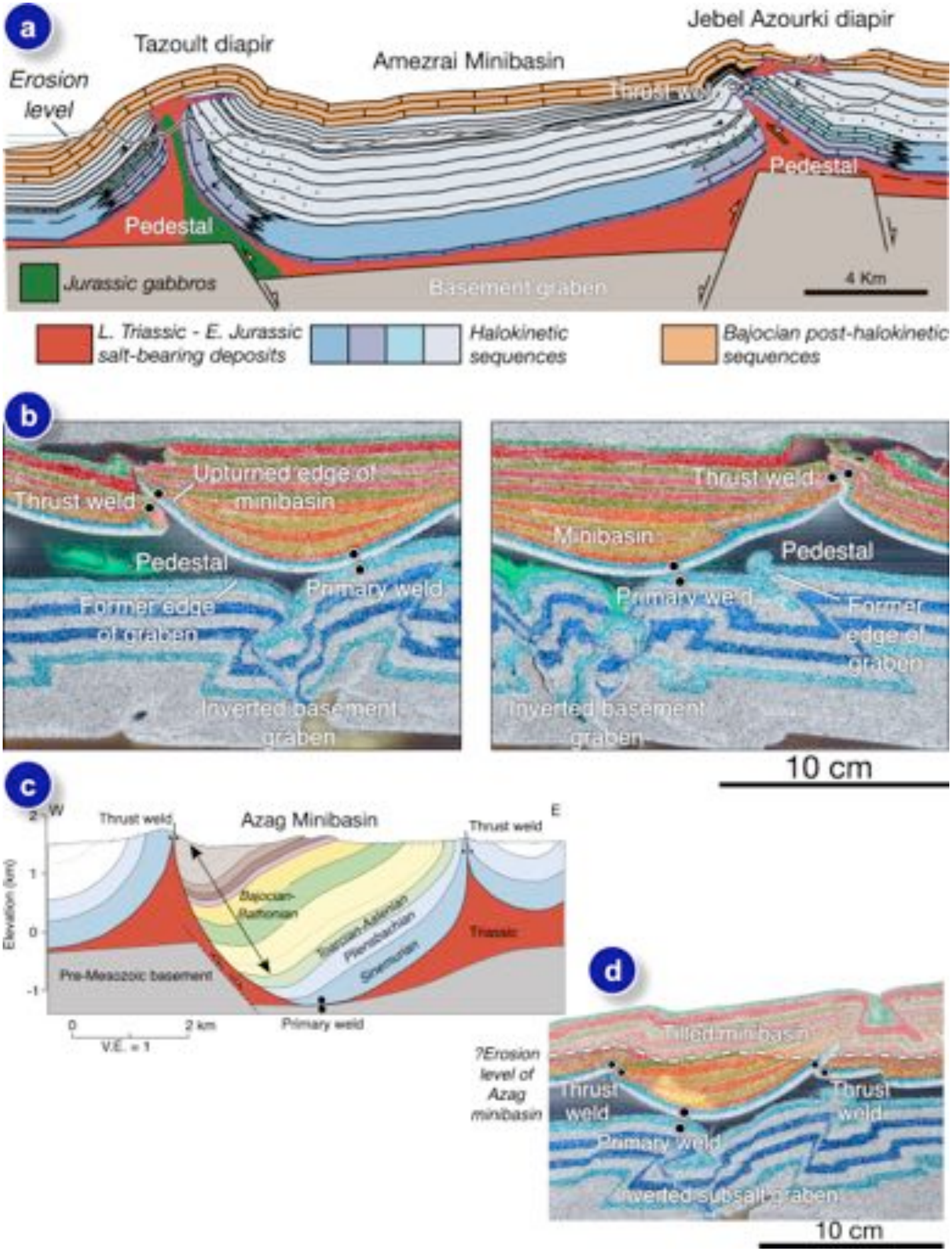
a
Jebel Azourki diapir
Tazoult diapir
Amezrai Minibasin
Erosion level
Thrust weld
Pedestal
Pedestal
Jurassic gabbros
Basement graben
4 Km
L. Triassic - E. Jurassic salt-bearing deposits
Halokinetic sequences
Bajocian post-halokinetic sequences
b
Upturned edge of minibasin
Thrust weld
Pedestal
Primary weld
Former edge of graben
Inverted basement graben
Thrust weld
Minibasin
Pedestal
Primary weld
Former edge of graben
Inverted basement graben
10 cm
c
W
E
Thrust weld
Azag Minibasin
Thrust weld
Elevation (km)
Bajocian-Rathonian
Toarcian-Aalenian
Pliensbachian
Sinemurian
Triassic
Pre-Mesozoic basement
Primary weld
0
2 km
V.E. = 1
d
?Erosion level of Azag minibasin
Tilted minibasin
Thrust weld
Thrust weld
Primary weld
Inverted subsalt graben
10 cm